Title: An adult clock component links circadian rhythms to pancreatic β-cell maturation

Authors:

Ana P. Montalvo[1], Zoe L. Gruskin[2, 3], Andrew Leduc[4], Mai Liu[3, 5], Zihan Gao[3, 5], June H. Ahn[3], Juerg R. Straubhaar[6], Nikolai Slavov[4], and Juan R. Alvarez-Dominguez[2, 3]

Affiliations:

[1] Department of Neurosurgery, Brigham and Women's Hospital, Boston, MA 02115, USA

[2] Department of Cell and Developmental Biology, University of Pennsylvania Perelman School of Medicine, Philadelphia, PA 19104, USA

[3] Institute for Regenerative Medicine and Institute for Diabetes, Obesity and Metabolism, University of Pennsylvania Perelman School of Medicine, Philadelphia, PA 19104, USA

[4] Departments of Bioengineering and Biology, Single-Cell Proteomics Center and Barnett Institute, Northeastern University, Boston, MA 02115, USA

[5] Department of Bioengineering, University of Pennsylvania Perelman School of Medicine, Philadelphia, PA 19104, USA

[6] Bioinformatics Center, Massachusetts Eye and Ear Infirmary, Boston, MA 02114, USA

*Correspondence: Juan.Alvarez@pennmedicine.upenn.edu

Abstract:

How ubiquitous circadian clocks orchestrate tissue-specific outputs is not well understood. Pancreatic β cell-autonomous clocks attune insulin secretion to daily energy cycles, and desynchrony from genetic or behavioral disruptions raises type 2 diabetes risk. We show that the transcription factor DEC1, a clock component induced in adult β cells, coordinates their glucose responsiveness by synchronizing energy metabolism and secretory gene oscillations. *Dec1*-ablated mice develop lifelong hypo-insulinemic diabetes, despite normal islet formation and intact circadian *Clock* and *Bmal1* activators. DEC1, but not CLOCK/BMAL1, binds maturity-linked genes that mediate respiratory metabolism and insulin exocytosis, and *Dec1* loss disrupts their transcription synchrony. Accordingly, β-cell *Dec1* ablation causes hypo-insulinemia due to immature glucose responsiveness, dampening insulin rhythms. Thus, Dec1 links circadian clockwork to the β-cell maturation process, aligning metabolism to diurnal energy cycles.

Main Text

Optimizing energy utilization to fuel availability is critical for metabolic homeostasis (*1*). In mammals, cell-autonomous 24-hour clocks throughout the body align tissue functions to daily feeding-fasting cycles, and misalignment from genetic or behavioral perturbation triggers metabolic dysfunction, fueling type 2 diabetes risk (*2*). Circadian clocks comprise a core feedback loop between transcription activators (CLOCK/BMAL1) and repressors (PERs/CRYs) and interlocking loops involving the ROR, REV-ERB, and DEC proteins (*3*). However, major questions remain as to how core/interlocking components synchronize distinct genes in distinct tissues to coordinate overall metabolism.

To dissect the regulation of metabolism by cell type and state specific clock components, we focused on pancreatic β cells, vital controllers of glucose homeostasis (*4*). We studied DEC1/2 (also named BHLHE40/41, SHARP2/1) since they partake in the transcriptional regulatory circuit that defines mature β-cell identity (*5*). Here, we define DEC targets in β cells and investigate their role in the diurnal control of insulin secretion and metabolic homeostasis.

Circadian clock DEC components define mature β cells and control glucose homeostasis

We found that DEC1/2 expression discerns mature (juvenile/adult) from immature (fetal/ neonatal) β-cells in mouse, rat, pig, and human (fig. S1). Notably, *Dec1*'s specificity for adult β-cells is highly conserved, second only to *Mafa*, a master driver of mature β-cell physiology (*6, 7*), among adult-restricted transcription factors regulating human β-cell maturation (Fig. 1A). Physiologic β-cell *Dec1/2* expression shows 24-hour periodicity (Fig. 1B), consistent with roles in circadian clockwork. To establish whether embryonic *Dec* ablation hinders metabolism, we examined glucose homeostasis in *Dec1*$^{-/-}$ and *Dec2*$^{-/-}$ mice (*8, 9*) and their wild-type littermates. Though these mice display normal weight, body composition, and insulin sensitivity (fig. S2, C to E), *Dec1*$^{-/-}$ mice show striking hyperglycemia and glucose intolerance at 2-3 and 8 months of age (Fig. 1, C and D, and fig. S2, A, B, and P). *Dec2*$^{-/-}$ mice, conversely, trend toward lower blood glucose and faster glucose clearance. We verified normal food intake and patterns of activity and energy expenditure, with delayed phase onset but sustained period length (fig. S2, F to O), in both *Dec* mutants. Yet, *Dec1*$^{-/-}$ mice show low energy expenditure during the active phase, consistent with a hypometabolic state. By contrast, *Dec2*$^{-/-}$ mice exercise more, consistent with improved glucose handling. A primary defect in β-cell function was further supported by selective impairment of glucose-stimulated insulin secretion (GSIS) in *Dec1*$^{-/-}$ mice (Fig. 1E), despite normal islet mass, architecture, and proliferation (fig. S2, Q to T). These data implicate

the DEC transcription factors as cycling adult β cell clock components regulating glucose homeostasis and metabolism.

Rhythmic energy metabolism and secretory genes are selectively bound by DEC clock components

To better understand how DECs tune β-cell function, we determined their genome-wide binding via chromatin immunoprecipitation-sequencing in the mouse β cell line Beta-TC6. As expected, DEC1/2 bind CACGTG E-box motifs with significant overlap, preferentially at promoters, including for core clock activators (*Clock/Bmal1*) and repressors (*Per*/*Cry*) and interlocking loop *Ror*, *Rev-erb*, and *Dec* genes (Fig. 2A and fig. S3, A to E). Among DEC1/2 binding sites, 26% (2,179) are also bound by CLOCK/BMAL1 in Beta-TC6 cells (*10*) (Fig. 2, B and C), consistent with competition for E-box binding (*11*), and enrich for clock and NOTCH/TGF-β signaling effectors (fig. S3F). Surprisingly, non-shared DEC1/2 and CLOCK/ BMAL1 binding sites target largely distinct gene pathways (Fig. 2D and fig. S3F). The DEC1/2-specific cistrome enriches for β-cell development regulators, including the key maturity controllers *Neurod1* and *Mafa* (*6, 12*); energy metabolism effectors like *Glut2* and *ChREBP* that enact β-cell glucose import (*13*) and mitogenic signaling (*14*); and components of insulin signaling (*Insr, Irs1, Igf2*) and vesicle membrane docking/fusion, including many voltage-gated K/Ca^{2+} channel subunits, calmodulins/ Ca^{2+}-dependent kinases, and SNAREs (*Vamp2/3, Stx4a/6/16, Stxbp1/5l/6, Snap25/91/in*). The specific targets of CLOCK/BMAL1, by contrast, enrich for cAMP-coupled signaling mediators of vesicle budding that are often co-bound by PDX1, as reported and consistent with impaired GPCR-stimulated insulin release in *Bmal1*-disrupted mice (*10*).

To examine rhythmicity among DEC-bound gene targets, we performed RNA-sequencing around the 24-hour clock in islets isolated from wild-type mice and used dryR (*15*) for Bayesian

statistics-based rhythm model selection (materials and methods). DEC1/2 targets show pervasive circadian oscillation, comprising ~73% of bound and expressed genes, comparable to ~72% for CLOCK/BMAL1 targets, which co-varied in amplitude and significance values (Fig. 2E and fig. S3G). Notably, cyclic DEC targets include regulators of β-cell development, energy metabolism, and insulin secretion (see below), which also oscillate in human islets (*5, 10, 16*). These findings implicate DEC1/2 in discrete steps of glucose-triggered insulin secretion, through the selective binding of rhythmic genes mediating glucose and insulin metabolism in mature β cells.

β-cell DEC1 disruption causes glucose intolerance and hypoinsulinemia due to immature islet function

Prompted by the diabetic phenotypes of *Dec1*$^{-/-}$ mice, we next sought to ascertain the direct role of β-cell DEC1 in metabolic homeostasis by generating *InsCre Dec1*$^{flx/flx}$ (βKO) mice. Despite >60% reduced *Dec1* expression, βKO mice display normal islet anatomy, number, proliferation, and insulin content (Fig. 3A and fig. S4, A to F). Remarkably, these mice develop severe glucose intolerance across day and night, relative to wild-type or heterozygous littermates, at a young age (3-4 months), persisting in 8-month-olds (Fig. 3B and fig. S4G). Though their weight and insulin sensitivity is normal (fig. S4, H and I), βKO mice are hypo-insulinemic, with markedly reduced glucose-stimulated and *ad libitum* insulin throughout the day, including stunted insulin ascent at the start of the feeding period (Fig. 3, C and D). Further, our isolated islet studies reveal impaired kinetics and magnitude of glucose-coupled insulin release (Fig. 3E and fig. S4J). Thus, β-cell specific *Dec1* ablation disrupts islet insulin secretion, rendering mice glucose intolerant.

Insulin secretion matures postnatally, as secretory capacity and the glucose threshold for release increase (*17, 18*). To better define the defective step in βKO islet function, we examined their responses across glucose levels. Isolated βKO islets show high insulin secretion at basal

glucose levels, with full insulin responses between 0.5 mM (baseline) and 2.8-5 mM (low) glucose (Fig. 3F and fig. S4, J and K), evidencing a lower glucose threshold for insulin release. As responses to high (20mM) glucose are markedly reduced, despite normal insulin content and exocytosis upon depolarization with KCl (Fig. 3, E and F, and fig. S4J), these results indicate that β-cell *Dec1* loss causes hypo-insulinemia due to immature glucose responsiveness.

DEC1 synchronizes respiratory metabolism and insulin secretion gene rhythms in pancreatic β cells

To establish how genomic regulation by DEC1 controls GSIS maturity, we examined the impact of β-cell *Dec1* ablation on gene expression patterns. RNA-sequencing around the 24-hour clock in islets isolated from *Dec1*-βKO mice revealed 3,176 genes (13% of all detected) with altered rhythmicity (Fig. 4A, fig. S5A, and Table S2). Rhythm-disrupted genes enriched for vesicular transport and epigenetic regulation, including *Bmal1*, though other core clock genes were not affected as much (fig. S5, F and G). We also found 818 genes that become rhythmic with high amplitudes, involving general machinery and calcium signaling mediators for vesicle budding. Unexpectedly, specific GSIS regulators retained diurnal cycling but became phase shifted (Fig. 4A and fig. S5, C to E). These included effectors of glucose sensing (*Glut2*, *Foxo1*) and metabolism (TCA, electron transport chain, ATP synthesis enzymes); PI3K-Akt-mTOR signaling mediators regulating energy homeostasis (*Gsk3b, Igf1*); and direct effectors of insulin transport (tubulins, ARF/RAB GTPases) and exocytosis (G-protein subunits, *Irs1/2, Syt4/13*). Discordant phase shifts, such as *Glut2*/*Igf1* phase delay and prevalent respiratory enzyme phase advances, caused marked desynchrony between energy metabolism and GSIS gene oscillations (Fig. 4, B and C, and fig. S5E). As DEC1 binding is overrepresented among rhythm-shifted genes (Fig. 4D

and fig. S5B), these findings indicate that gene-level temporal control by DEC1 mainly acts to synchronize insulin responses to glucose sensing and oxidative metabolism in mature β cells.

Pancreatic islets rely on temporally orchestrated interactions between heterogenous cell types to sustain glucose homeostasis (*19, 20*). To better understand the effects of β-cell clock disruption, we performed single-cell RNA-sequencing (scRNA-seq), single-cell proteomic mass spectrometry (SCoPE-MS) (*21, 22*), and single-cell assay for transposase-accessible chromatin using sequencing (scATAC-seq) in *Dec1*-βKO islets. Marker-based cross-modal integration (*23*) (materials and methods) clearly identified α, δ, γ, stellate, vascular, and immune cells, along with β-cell subpopulations with low/high hormone (*Ins, Chga, Iapp, Ucn3*) expression/promoter accessibility (Fig. 4E and fig. S6). While the ratio of these cell types was largely unchanged, we found pervasive chromatin and expression-level gene deregulation across low/high hormone β-cell states, enriched for energy metabolism and GSIS regulation (fig. S7A). We verified that these changes remodel the proteome, as the single-cell proteomic data revealed marked deregulation of proteins mediating glucose metabolism (TCA, OXPHOS enzymes) and GSIS (insulin processing, transport, and secretion) in β-cells (fig. S7, B to D).

We next sought to examine to which extent altered gene expression impacts rhythmicity. Most deregulated genes lack or maintain cyclic expression in *Dec1*-βKO islets (fig. S7E). Yet, specific subsets, overrepresented for GSIS effectors, show both altered rhythmicity and mean expression level, with exocytic machinery concurrently upregulated and phase-shifted in rhythm (fig. S7F). To establish direct transcriptional regulation by DEC1, we intersected deregulated and rhythm-altered genes with the DEC1 cistrome. This identified 31 direct targets, specifically enriched for glucose responsiveness and insulin secretion, that define the core DEC1 pathway in β-cells (Fig. 4, F and G, and Table S2). Notably, these include key β-cell maturity transcription

factors *Mafa* (*6, 7*) and *Hif1a* (*24*), the G_o-type G protein–coupled receptor subunit *Gnao1*, and the exocyst co-factor *Wash1c* (*25*) as the DEC1 targets linking glucose responsiveness to insulin discharge.

Finally, we tested the ability of insulinotropic agents to rescue the GSIS defect of isolated *Dec1*-βKO islets. Glucose stimulation together with the Ca^{2+} ionophore ionomycin or with adenylate cyclase agonists (forskolin, 8-br-cAMP) did not restore insulin secretion (Fig. 4H and fig. S7G), consistent with disrupted calcium-dependent and cAMP-coupled GPCR signaling. Strikingly, GSIS was restored when these steps were bypassed by PKC-dependent signaling stimulation, with the direct activator PMA (phorbol 12-myristate 13-acetate) or through the muscarinic receptor agonist carbachol (Fig. 4H and fig. S7G). PKC stimulates GSIS via SNAP25 and MUNC13/18 (*26*), mediators of insulin exocytosis that show rhythmic but asynchronous/ lower levels in *Dec1*-βKO islets (fig. S5G). Thus, PKC activation can relieve deregulated cycling of late secretory machinery due to β-cell *Dec1* loss, revealing a molecular path for its temporal control of β-cell GSIS and homeostasis.

Discussion

We have defined a genomic basis for the coordination of physiologic metabolism by adult β cell-specific circadian clockwork. Rhythmic tissue physiology is thought to be programmed by ubiquitous CLOCK/BMAL1 activators partnering with lineage-restricted transcription factors (*27, 28*), consistent with the phenotypes of conditional knockouts. Yet, not all cyclic genes are CLOCK/BMAL1 targets, and such mutants may be disrupted for the entire circadian pathway (*29*). Using pancreatic β-cells as a model for cell type-specific clock regulation of metabolism,

we find discrete roles for core CLOCK/BMAL1 and adult-restricted DEC1/2 regulators in programming energy metabolism and secretory gene oscillations that drive diurnal variation in the glucose responsiveness of insulin secretion.

Our genomic binding studies illuminate how tissue-specific clock outputs are generated. Though CLOCK/BMAL1 and DEC1/2 recognize E-box motifs and bind clock genes, including each other's, most of their targets are distinct. CLOCK/BMAL1 preferentially target sites co-bound by the pancreatic lineage-determining factor PDX1 (*10*), enriched for late secretory genes, while DEC1/2 target specific metabolic/signaling mediators of insulin responses to glucose. As both sets of targets show robust rhythms, our findings evidence modular control of local clock outputs, with cell state-restricted gene rhythms set mainly via interlocking loop controllers rather than core clock factors directly (*30, 31*). Further studies will be needed to establish the basis for these factors accessing distinct E-boxes in the same cell type and across diverse tissues (*32, 33*).

Our finding that disrupting *Dec1* is sufficient to cause lifelong hypo-insulinemic diabetes, recalling diabetic phenotypes upon pancreas *Bmal1* loss but without stunted islet growth/survival as seen in embryonic mutants (*34, 35*), suggests that diurnal insulin control operates mainly via this arm of the clock. Our studies further reveal that *Dec1* loss renders islets refractory to glucose stimulation in part due to a diminished threshold for insulin release, evoking fetal/neonatal islets (*17, 18*). Given DEC1's adult-restricted induction and direct control of β-cell maturity genes, these observations establish a molecular link between the 24-hour clock and acquisition of the mature β-cell phenotype.

Finally, we show that synchrony of energy metabolism pathways is critical for the coordination of local physiology by cell type-specific clockwork. Aligning tissue functions to energy cycles offers a fitness advantage (*1, 2*). As clocks are activated in metabolic tissues during

the onset of feeding-fasting rhythms (*36, 37*), an intriguing possibility is that they unlock phenotypic maturity by optimizing specialized tasks to daily energy availability (*38*). Inability to anticipate these cycles, due to clock or circadian disruption (*39, 40*), may in turn cause metabolic dysfunction through the loss of mature cell phenotypes. The finding that daily control of insulin secretion and glucose homeostasis throughout life requires the DEC1 clock component induced in mature β cells provides further insight into how their specialized function is achieved. Given major interest in furthering maturation of *in vitro*-derived human islets for diabetes modeling and therapy (*41, 42*), the fact that DEC1 defines β-cell maturity from rodents to human opens a new window for co-opting rhythms to attain fully functional β-cells for human research and medicine.

References and Notes

1. S. Panda, Circadian physiology of metabolism. *Science* **354**, 1008-1015 (2016).
2. J. Bass, M. A. Lazar, Circadian time signatures of fitness and disease. *Science* **354**, 994-999 (2016).
3. E. E. Zhang, S. A. Kay, Clocks not winding down: unravelling circadian networks. *Nat Rev Mol Cell Biol* **11**, 764-776 (2010).
4. K. H. Kaestner *et al.*, What is a beta cell? - Chapter I in the Human Islet Research Network (HIRN) review series. *Mol Metab* **53**, 101323 (2021).
5. J. R. Alvarez-Dominguez *et al.*, Circadian Entrainment Triggers Maturation of Human In Vitro Islets. *Cell Stem Cell* **26**, 108-122 e110 (2020).
6. Y. Hang *et al.*, The MafA transcription factor becomes essential to islet beta-cells soon after birth. *Diabetes* **63**, 1994-2005 (2014).
7. C. Aguayo-Mazzucato *et al.*, Mafa expression enhances glucose-responsive insulin secretion in neonatal rat beta cells. *Diabetologia* **54**, 583-593 (2011).
8. X. Jiang *et al.*, BHLHB2 controls Bdnf promoter 4 activity and neuronal excitability. *J Neurosci* **28**, 1118-1130 (2008).
9. M. J. Rossner *et al.*, Disturbed clockwork resetting in Sharp-1 and Sharp-2 single and double mutant mice. *PLoS One* **3**, e2762 (2008).
10. M. Perelis *et al.*, Pancreatic beta cell enhancers regulate rhythmic transcription of genes controlling insulin secretion. *Science* **350**, aac4250 (2015).
11. S. Honma *et al.*, Dec1 and Dec2 are regulators of the mammalian molecular clock. *Nature* **419**, 841-844 (2002).
12. C. Gu *et al.*, Pancreatic beta cells require NeuroD to achieve and maintain functional maturity. *Cell Metab* **11**, 298-310 (2010).
13. M. T. Guillam *et al.*, Early diabetes and abnormal postnatal pancreatic islet development in mice lacking Glut-2. *Nat Genet* **17**, 327-330 (1997).

14. M. R. Metukuri *et al.*, ChREBP mediates glucose-stimulated pancreatic beta-cell proliferation. *Diabetes* **61**, 2004-2015 (2012).
15. B. D. Weger *et al.*, Systematic analysis of differential rhythmic liver gene expression mediated by the circadian clock and feeding rhythms. *Proc Natl Acad Sci U S A* **118**, (2021).
16. C. Saini *et al.*, A functional circadian clock is required for proper insulin secretion by human pancreatic islet cells. *Diabetes Obes Metab* **18**, 355-365 (2016).
17. B. Blum *et al.*, Functional beta-cell maturation is marked by an increased glucose threshold and by expression of urocortin 3. *Nat Biotechnol* **30**, 261-264 (2012).
18. C. Aguayo-Mazzucato, C. Sanchez-Soto, V. Godinez-Puig, G. Gutierrez-Ospina, M. Hiriart, Restructuring of pancreatic islets and insulin secretion in a postnatal critical window. *PLoS One* **1**, e35 (2006).
19. J. T. Walker, D. C. Saunders, M. Brissova, A. C. Powers, The Human Islet: Mini-Organ With Mega-Impact. *Endocr Rev* **42**, 605-657 (2021).
20. G. M. Noguchi, M. O. Huising, Integrating the inputs that shape pancreatic islet hormone release. *Nat Metab* **1**, 1189-1201 (2019).
21. B. Budnik, E. Levy, G. Harmange, N. Slavov, SCoPE-MS: mass spectrometry of single mammalian cells quantifies proteome heterogeneity during cell differentiation. *Genome Biol* **19**, 161 (2018).
22. A. Leduc, R. G. Huffman, J. Cantlon, S. Khan, N. Slavov, Exploring functional protein covariation across single cells using nPOP. *Genome Biol* **23**, 261 (2022).
23. T. Stuart *et al.*, Comprehensive Integration of Single-Cell Data. *Cell* **177**, 1888-1902 e1821 (2019).
24. J. Yang *et al.*, Early postnatal activation of the hypoxia pathway disrupts β-cell function. *bioRxiv*, 2021.2006.2009.447705 (2021).
25. P. Monteiro *et al.*, Endosomal WASH and exocyst complexes control exocytosis of MT1-MMP at invadopodia. *J Cell Biol* **203**, 1063-1079 (2013).
26. A. J. Trexler, J. W. Taraska, Regulation of insulin exocytosis by calcium-dependent protein kinase C in beta cells. *Cell Calcium* **67**, 1-10 (2017).
27. J. R. Beytebiere, B. J. Greenwell, A. Sahasrabudhe, J. S. Menet, Clock-controlled rhythmic transcription: is the clock enough and how does it work? *Transcription* **10**, 212-221 (2019).
28. J. S. Takahashi, Transcriptional architecture of the mammalian circadian clock. *Nat Rev Genet* **18**, 164-179 (2017).
29. K. B. Koronowski, P. Sassone-Corsi, Communicating clocks shape circadian homeostasis. *Science* **371**, (2021).
30. A. C. Liu *et al.*, Redundant function of REV-ERBalpha and beta and non-essential role for Bmal1 cycling in transcriptional regulation of intracellular circadian rhythms. *PLoS Genet* **4**, e1000023 (2008).
31. Y. H. Kim, M. A. Lazar, Transcriptional Control of Circadian Rhythms and Metabolism: A Matter of Time and Space. *Endocr Rev* **41**, 707-732 (2020).
32. T. Kreslavsky *et al.*, Essential role for the transcription factor Bhlhe41 in regulating the development, self-renewal and BCR repertoire of B-1a cells. *Nat Immunol* **18**, 442-455 (2017).
33. E. P. Consortium, An integrated encyclopedia of DNA elements in the human genome. *Nature* **489**, 57-74 (2012).
34. B. Marcheva *et al.*, Disruption of the clock components CLOCK and BMAL1 leads to hypoinsulinaemia and diabetes. *Nature* **466**, 627-631 (2010).
35. K. Rakshit, T. W. Hsu, A. V. Matveyenko, Bmal1 is required for beta cell compensatory expansion, survival and metabolic adaptation to diet-induced obesity in mice. *Diabetologia* **59**, 734-743 (2016).
36. L. Bideyan, R. Nagari, P. Tontonoz, Hepatic transcriptional responses to fasting and feeding. *Genes Dev* **35**, 635-657 (2021).

37. K. Rakshit *et al.*, Postnatal Ontogenesis of the Islet Circadian Clock Plays a Contributory Role in beta-Cell Maturation Process. *Diabetes* **67**, 911-922 (2018).
38. J. R. Alvarez-Dominguez, D. A. Melton, Cell maturation: Hallmarks, triggers, and manipulation. *Cell* **185**, 235-249 (2022).
39. J. Bass, J. S. Takahashi, Circadian integration of metabolism and energetics. *Science* **330**, 1349-1354 (2010).
40. Y. Gao *et al.*, Association between shift work and risk of type 2 diabetes mellitus: a systematic review and dose-response meta-analysis of observational studies. *Chronobiol Int* **37**, 29-46 (2020).
41. N. J. Hogrebe, M. Ishahak, J. R. Millman, Developments in stem cell-derived islet replacement therapy for treating type 1 diabetes. *Cell Stem Cell* **30**, 530-548 (2023).
42. K. F. Leavens, J. R. Alvarez-Dominguez, L. T. Vo, H. A. Russ, A. V. Parent, Stem cell-based multi-tissue platforms to model human autoimmune diabetes. *Mol Metab* **66**, 101610 (2022).
43. C. Postic *et al.*, Dual roles for glucokinase in glucose homeostasis as determined by liver and pancreatic beta cell-specific gene knock-outs using Cre recombinase. *J Biol Chem* **274**, 305-315 (1999).
44. A. I. Mina *et al.*, CalR: A Web-Based Analysis Tool for Indirect Calorimetry Experiments. *Cell Metab* **28**, 656-666 e651 (2018).
45. D. S. Li, Y. H. Yuan, H. J. Tu, Q. L. Liang, L. J. Dai, A protocol for islet isolation from mouse pancreas. *Nat Protoc* **4**, 1649-1652 (2009).
46. A. Dobin *et al.*, STAR: ultrafast universal RNA-seq aligner. *Bioinformatics* **29**, 15-21 (2013).
47. Y. Zhang *et al.*, Model-based analysis of ChIP-Seq (MACS). *Genome Biol* **9**, R137 (2008).
48. H. M. Amemiya, A. Kundaje, A. P. Boyle, The ENCODE Blacklist: Identification of Problematic Regions of the Genome. *Sci Rep* **9**, 9354 (2019).
49. A. R. Quinlan, I. M. Hall, BEDTools: a flexible suite of utilities for comparing genomic features. *Bioinformatics* **26**, 841-842 (2010).
50. D. E. Newburger, M. L. Bulyk, UniPROBE: an online database of protein binding microarray data on protein-DNA interactions. *Nucleic Acids Res* **37**, D77-82 (2009).
51. A. Sandelin, W. Alkema, P. Engstrom, W. W. Wasserman, B. Lenhard, JASPAR: an open-access database for eukaryotic transcription factor binding profiles. *Nucleic Acids Res* **32**, D91-94 (2004).
52. A. Jolma *et al.*, DNA-binding specificities of human transcription factors. *Cell* **152**, 327-339 (2013).
53. P. Machanick, T. L. Bailey, MEME-ChIP: motif analysis of large DNA datasets. *Bioinformatics* **27**, 1696-1697 (2011).
54. T. L. Bailey, P. Machanick, Inferring direct DNA binding from ChIP-seq. *Nucleic Acids Res* **40**, e128 (2012).
55. S. Gupta, J. A. Stamatoyannopoulos, T. L. Bailey, W. S. Noble, Quantifying similarity between motifs. *Genome Biol* **8**, R24 (2007).
56. Y. Zhou *et al.*, Metascape provides a biologist-oriented resource for the analysis of systems-level datasets. *Nat Commun* **10**, 1523 (2019).
57. S. Anders, P. T. Pyl, W. Huber, HTSeq--a Python framework to work with high-throughput sequencing data. *Bioinformatics* **31**, 166-169 (2015).
58. S. Anders, W. Huber, Differential expression analysis for sequence count data. *Genome Biol* **11**, R106 (2010).
59. R. Zhang, A. A. Podtelezhnikov, J. B. Hogenesch, R. C. Anafi, Discovering Biology in Periodic Data through Phase Set Enrichment Analysis (PSEA). *J Biol Rhythms* **31**, 244-257 (2016).
60. A. Helman *et al.*, A Nutrient-Sensing Transition at Birth Triggers Glucose-Responsive Insulin Secretion. *Cell Metab* **31**, 1004-1016 e1005 (2020).

61. M. D. Luecken, F. J. Theis, Current best practices in single-cell RNA-seq analysis: a tutorial. *Mol Syst Biol* **15**, e8746 (2019).
62. J. Chiou *et al.*, Single-cell chromatin accessibility identifies pancreatic islet cell type- and state-specific regulatory programs of diabetes risk. *Nat Genet* **53**, 455-466 (2021).
63. B. Li, C. N. Dewey, RSEM: accurate transcript quantification from RNA-Seq data with or without a reference genome. *BMC Bioinformatics* **12**, 323 (2011).
64. N. Sharon *et al.*, A Peninsular Structure Coordinates Asynchronous Differentiation with Morphogenesis to Generate Pancreatic Islets. *Cell* **176**, 790-804 e713 (2019).
65. M. D. Robinson, D. J. McCarthy, G. K. Smyth, edgeR: a Bioconductor package for differential expression analysis of digital gene expression data. *Bioinformatics* **26**, 139-140 (2010).
66. C. S. Ross-Innes *et al.*, Differential oestrogen receptor binding is associated with clinical outcome in breast cancer. *Nature* **481**, 389-393 (2012).
67. H. Specht *et al.*, Automated sample preparation for high-throughput single-cell proteomics. *bioRxiv*, 399774 (2018).
68. A. A. Petelski *et al.*, Multiplexed single-cell proteomics using SCoPE2. *Nat Protoc* **16**, 5398-5425 (2021).
69. H. Specht *et al.*, Single-cell proteomic and transcriptomic analysis of macrophage heterogeneity using SCoPE2. *Genome Biol* **22**, 50 (2021).
70. H. Specht, N. Slavov, Optimizing Accuracy and Depth of Protein Quantification in Experiments Using Isobaric Carriers. *J Proteome Res* **20**, 880-887 (2021).
71. J. Liu *et al.*, Jointly defining cell types from multiple single-cell datasets using LIGER. *Nat Protoc* **15**, 3632-3662 (2020).
72. L. Gatto *et al.*, Initial recommendations for performing, benchmarking and reporting single-cell proteomics experiments. *Nat Methods* **20**, 375-386 (2023).

Acknowledgments:

We thank Douglas A. Melton for his generous support during the initial stage of this project, and Daria Zhadanova, Monica Cho, Israeli M. Galicia-Silva, and Samuel D. Pollock for assistance with bioinformatics and graphics; the Beth Israel Deaconess Medical Center Metabolic Core, Harvard Medical School Biopolymers Facility, University of Pennsylvania Laboratory Animal resources, and Harvard University Bauer Core sequencing facility for technical support and critical discussions; and Mitchell A. Lazar, Amita Sehgal, Kenneth S. Zaret and members of the Alvarez-Dominguez laboratory for critical feedback on this manuscript.

Funding: This work was supported by grants from the NIH (K01DK129442, the Human Islet Research Network (U24DK104162), start-up funding from the Perelman School of

Medicine at the University of Pennsylvania, and by a pilot award from the Diabetes Research Center at the University of Pennsylvania (P30DK19525) to J.R.A-D., who was also supported by a Howard Hughes Medical Institute Life Sciences Research Foundation Fellowship; and by grants to Douglas A. Melton from the JDRF (5-COE-2020-967-M-N), and the JPB Foundation (award no. 1094).

Author contributions: A.P.M., Z.L.G., A.L., and J.RA.-D. performed experiments. A.L., M.L., Z.G., J.H.A., J.R.S., and J.RA.-D. conducted bioinformatics analyses. A.P.M., Z.L.G., N.S., and J.RA.-D. designed the research, interpreted the results, and wrote the manuscript.

Competing interests: Authors declare that they have no competing interests.

Data and materials availability: Proteomic raw data are deposited at MassIVE (MSV000092610). Processed proteomic data can be accessed at https://shorturl.at/DNWY8.

Supplementary Materials

Materials and Methods
Supplementary Text
Figs. S1 to S7
Tables S1 to S2
References (*40–65*)

Materials and Methods

Animals

Male *Dec1*$^{-/-}$ (*8*) and *Dec2*$^{-/-}$ (*9*) mice were produced and maintained on a C57BL/6J background. *Dec1*$^{f/f}$ mice (kindly provided by Dr. Lino Tessarollo, National Institutes of Health) (*8*) were crossed to *InsCre* mice (kindly provided by Dr. Douglas Melton, Harvard University) (*43*) to generate *InsCre Dec1*$^{f/f}$ mice and littermate controls. Unless otherwise noted, all mice were housed on a 12-hours light:12-hours dark cycle (lights on at 6am [zeitgeber time 0, ZT0] and lights off at 6pm [ZT12]) with continuous access to regular chow and water. All animal care and use procedures followed the guidelines of the Institutional Animal Care and Use Committee of the University of Pennsylvania in accordance with the guidelines of the NIH.

Glucose/insulin measurements

Blood glucose levels were measured via tail vein bleed using a OneTouch Ultra2 glucometer (LifeScan). Plasma samples were collected via tail vein bleed into a Microvette CB300 (Sarstedt, Inc.) capillary tube. Insulin concentration was quantified using a Mouse Ultrasensitive Insulin ELISA kit (ALPCO Diagnostics) within 24 hours of sample collection.

Glucose and insulin tolerance tests

Glucose tolerance tests were conducted in mice fasted for 16 hours. Blood glucose levels were measured as indicated above following intraperitoneal injection of room-temperature D-(+)-glucose in 0.9% sterile saline at 2g/kg of body weight. Plasma insulin was measured as indicated above. Insulin tolerance tests were performed after a 4-hour fast, followed by intraperitoneal injection of 4°C insulin (*Humulin R*, Eli Lilly) in 0.9% sterile saline at 1U/kg of body weight.

Indirect calorimetry

Indirect calorimetry measurements were collected as described (*44*) with mice housed at 23°C in Promethion indirect calorimetry cages (Sable Systems) with free access to food and water. Mice were first assayed under regular light-dark cycles, with 6am-6pm light photoperiod. The first full 24-hour day was considered as an acclimation period, and the following 3 days used for data collection. Lights were then turned off in the chambers for dark-dark cycle measurements over 7 days, with food shaken down in days 2 and 4 at ZT4 . Body mass was measured before and after the experiment, and the average was used for regression analyses. Body mass composition was assessed by magnetic resonance imaging with an EchoMRI instrument before placing mice into metabolic cages. CalR analysis (RRID:SCR_015849) was performed as described (*44*).

Immunohistochemistry

Immunohistochemistry was performed as described previously (*5*). Mouse pancreata were fixed in 4% paraformaldehyde overnight at 4°C and kept in 70% ethanol. Fixed tissue was sectioned by the Penn Molecular Pathology and Imaging Core (RRID: SCR_022420). Sections were deparaffinized using Histoclear (Thermo Fisher Scientific; C78-2-G), submerged in 1X Citrate buffer (Sigma Aldrich; C9999-1000ML) for antigen retrieval, and placed in a pressure cooker for 30 minutes. Slides were blocked with 5% Donkey Serum (Jackson Immunoresearch; 017-000-121) and PBST (PBS and 0.3% Triton X-100 [Sigma Aldrich]) for 1 hour, then incubated with primary antibodies (Insulin: GB13121, Servicebio; Glucagon: GB13097, Servicebio; Ki67: 14-5698-82, eBioscience) diluted in PBST overnight at 4°C. The next morning, slides were washed twice with PBST and incubated with secondary antibodies at 1:500 dilution in PBST for 1 hour protected from light. Slides were subsequently washed twice and stained with 1x Trueblack

(Biotium; 23007) for 1 minute, followed by washing and incubating with PBS for 5 minutes. For imaging, slides were mounted with Prolong gold Antifade mount and with DAPI (Thermo Fisher Scientific; P36935), covered with coverslips and sealed with nail polish. Images were taken using a Zeiss LSM 510 microscope (Carl Zeiss).

Image analysis

ImageJ (NIH) was used to evaluate islet area, α and β cell area and relative proportions, and β cell proliferation. Islet area was calculated per mm^2 of pancreatic section area. α/β cell proportions were quantified as the fraction of Glucagon+/Insulin+ cells per islet, respectively. To quantify proliferating β cells, we calculated the ratio of Insulin+ Ki67+ cells to total Insulin+ cells within islets.

Islet isolation

Islet isolation was conducted as previously described (*45*), via *in situ* pancreas perfusion with 0.8 mg/ml collagenase P (Roche; 11-213-873-001) followed by pancreas digestion and islet purification using Histopaque 1077 and 1119 (Sigma). Islets were filtered through a 250 µm mesh filter, collected in a 40 µm mesh filter, and manually picked with a 200 µL micropipette, followed by overnight recovery in a 37°C 5% CO2 incubator prior to downstream experiments.

ChIP-sequencing

Chromatin immunoprecipitation-sequencing was conducted as described in (*5*), by incubating Beta-TC6 cells (ATCC; CRL-11506) cultured in DMEM supplemented with 15% FBS, 1% L-glutamine, and 1% penicillin/streptomycin with DEC1 (Novus Biologicals; NB100-1800) and

DEC2-V5 (GeneCopoeia, Inc. # EX-A4343-LX304) antibodies. Sequencing reads were mapped using STAR (*46*) with default parameters. Regions enriched for uniquely-mapped reads relative to input sample were called as binding peaks using MACS (*47*) with default parameters and "--pvalue=1e-9 --keep-dup=1", followed by filtering against overlap with problematic regions of the genome (*48*). Peaks from BMAL1, CLOCK, and PDX1 ChIP-sequencing in Beta-TC6 cells (*10*) were called in the same manner and concatenated and merged with DEC1 and DEC2 peaks using BEDTools (*49*) to obtain a unified peak catalog.

Motif enrichment

DNA sequences of DEC1 and DEC2 binding peaks were searched for enriched motifs from a database of vertebrate transcription factor recognition motifs(*50-52*) using MEME-ChIP (*53*) under Discriminative mode, which implements CentriMo (*54*) to identify centrally enriched motifs and tests for similarity to known motifs using Tomtom (*55*). Markov models of sequence nucleotide composition were used as the background model for motif matching to normalize for biased distribution of individual letters in the examined sequences.

Pathway enrichment

Gene lists ranked by a feature of interest (e.g., expression change, -log10 p-value of rhythmicity) were analyzed for enrichment of gene sets grouped by ontology annotations using Metascape (*56*) with default parameters, followed by curation of a representative term for each ranked annotation term cluster.

RNA-sequencing and differential expression

RNA-sequencing was conducted as described in (*5*). Sequencing reads were mapped using STAR (*46*) with default parameters. Read counts per gene were determined using HTSeq (*57*) and normalized using DESeq (*58*). We compared gene expression distributions (regardless of rhythmicity) between *Dec1* βKO and wild-type islets using DryR (*15*) (see below) to identify genes with differences in mean expression level, and considered genes with DESeq $p < 0.05$ in both the islet-level 24-hour time series and the β cell-level scRNA-seq data (see below) to be differentially expressed.

RNA rhythmicity analysis

RNA-sequencing data from *Dec1* βKO and wild-type islets was analyzed using DryR (*15*), which employs a Bayesian information criterion for rhythmicity and mean expression model selection, considering only genes with cumulative expression > 10 normalized counts across the 24-hour time series of either genotype. Default parameters were used to detect and estimate changes in amplitude, peak phase, and mean expression level between the two 24-hour series of $N = 7$ time-points with $n = 4$ replicate measurements each. To establish statistical confidence for a single condition, we used the dryseq_single function to calculate a p value for each gene. To quantify and compare rhythm phase shifts between *Dec1* βKO and wild-type islets for gene biological processes, we used PSEA (*59*), employing a significance threshold of $q < 0.05$ against a uniform phase distribution.

Islet glucose-stimulated insulin secretion

Insulin secretion assays were conducted in isolated islets as previously described (*5*). Islets were apportioned into four groups for triplicate GSIS assays and insulin content determination,

washed with Krebs buffer containing basal (0.5/2.8mM) glucose and loaded into 24-well plate inserts (Millicell Cell Culture Insert; PIXP01250), followed by pre-incubation in Krebs buffer with the same basal (0.5/2.8mM) glucose for 1h to remove residual insulin. Subsequently, islets were sequentially challenged with Krebs buffer containing indicated glucose concentrations with or without insulinotropic agents, with a 1h incubation for each treatment. Islets were then dissociated using TrypLE Express (Life Technologies) and cell counts were obtained using an automated cell counter (Beckman Coulter; Vi-Cell). All incubations were conducted at 37ºC, with supernatant samples collected at the end of each incubation.

Dynamic GSIS of handpicked, size-matched islets was conducted in triplicate as previously described (*5*) using an automated Perifusion System (BioRep). Chambers were first perifused with Krebs buffer containing basal (0.5/2.8mM) glucose for 1h at a flow rate of 100ul/min and sequentially with the indicated solutions for the indicated durations. Dynamic insulin secretion measurements were normalized to the mean of the first (basal) incubation.

Single-cell RNA and ATAC-sequencing

Isolated islets were gently dissociated using Accutase (StemCell Technologies), followed by single-cell capture, lysis, and RNA/ATAC library preparation with the 10x Chromium system (10x Genomics) using Single Cell 3' Gene expression (v3)/ATAC reagents following the manufacturer's instructions. Libraries were sequenced on a NovaSeq 4000 instrument (Illumina) and aligned to the mm10 reference genome assembly using Cell Ranger (10x Genomics) RNA/ATAC pipelines. Processing of mapped RNA reads was conducted as described previously (*60*) according to guidelines from (*61*) using Seurat V3 (*23*). ATAC reads were processed as described (*62*), filtering against low-quality fragments and excluding regions within non-

standard chromosomes or with extremely high (top 2%) nucleosome signal, to minimize noise and artifacts. Principal component analysis was performed on log-scaled counts for the top 4000 highly variable genes, and uniform manifold approximation and projection (UMAP) was computed with the top 50 principal components. Clusters were inferred using the Seurat "FindClusters" function adjusting for cluster resolution to optimize balance between cluster granularity and separation. Cross-modal integration of RNA and ATAC data was performed with Seurat (*23*) using the "FindTransferAnchors" and "TransferData" functions with a Canonical Correlation Analysis (CCA) dimension reduction method to transfer cluster identities from RNA to ATAC data. Cell clusters were assigned to cell types based on established islet cell identity markers (*23*).

Gene expression / promoter accessibility were computed for each cell type as expected counts within gene models / promoter-proximal (TSS ± 2kb) regions using RSEM (*63*). Differential expression / promoter accessibility was evaluated in β-cells as described (*64*) using edgeR (*65*). Uniquely-mapped reads were removed for duplicates and used for peak calling as described (*5*) using MACS2 (*47*) with default parameters and "–broad –qvalue 0.01", followed by filtering against very small (<20bp) or large (>10kb) peaks and against overlap with problematic regions of the genome (*48*). Differential peak counts were computed using DiffBind (*66*) with default settings.

Single-cell proteomics

Single-cell samples were prepared using the droplet nPOP method as detailed in (*22*). Sets of 14 single cells were run with a carrier sample of 100 cells of bulk digest labeled with TMT 126C

and a 5 cell reference labeled with TMT 127N prepared via mPOP sample preparation (*67, 68*). Channels 127C and 128N were not used due to isotopic contaminants from the carrier channel.

For LC/MS analysis, samples were separated via online nLC on a Dionex UltiMate 3000 UHPLC; 1 µl out of 1.1 µl of sample was loaded onto a 25 cm × 75 1 µm IonOpticks Aurora Series UHPLC column (AUR2-25075C18A). Buffer A was 0.1% formic acid in water and buffer B was 0.1% formic acid in 80% acetonitrile / 20% water. Samples were analyzed by a Q-Exactive mass spectrometer (Thermo Scientific). After a precursor scan from 450 to 1600 m/z at 70,000 resolving power, the top 7 most intense precursor ions were isolated for MS2 analysis via a 0.7 Th isolation window with a 0.3 Th offset. These ions were accumulated for at most 500 ms before being fragmented via HCD at a normalized collision energy of 33 eV (normalized to m/z 500, z = 1). The fragments were analyzed at 140,000 resolving power.

Single cell MS data was preprocessed via the SCoPE2 data pipeline (*69, 70*). Cell types were then assigned via label transfer performed with LIGER (*71*). Statistical tests between genotypes were performed via a t-test comparing protein expression between groups of single cells, using the Benjamini-Hochberg adjustment to correct for multiple hypotheses testing. Data and code are reported in accordance with community guidelines (*72*) and are available on github (https://github.com/SlavovLab/SC_Pancreas_KO).

Statistics

No statistical methods were used to predetermine sample size or remove outliers. To assess the statistical difference between two sets of unpaired data, a Shapiro-Wilk normality test was first performed via the shapiro.test R implementation with default parameters. Normally distributed data was then tested for equality of variance using the Bartlett.test R implementation with default

parameters. A two-sided t-test (t.test R implementation with default parameters and var.equal =FALSE or TRUE) was then used to assess confidence on the measured difference of their mean values. For unpaired data that did not follow a normal distribution, we used a non-parametric Wilcoxon rank sum test to determine if they belong to the same parent distribution.

Rigor and reproducibility

Mice from at least two independent littermate cohorts for each genotype were assayed for each experiment. All mice were housed individually for metabolic assays, with at least 1 week to recover between assays, including light/dark-phase measurements for the same cohort. Mice of all genotypes were assayed in parallel, blinded for genotype whenever possible, to minimize ascertainment bias. Differential gene regulation was validated across genomic/proteomic assays performed on independent mouse cohorts.

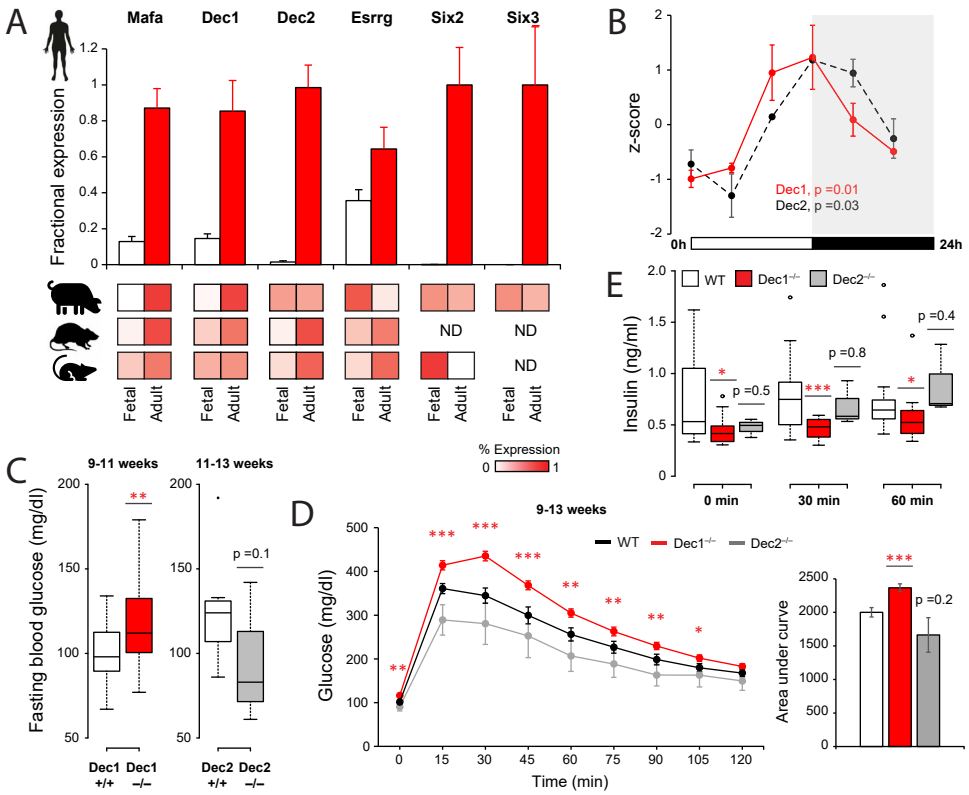

Fig. 1. Circadian clock DEC components mark mature β cells across species and control blood glucose homeostasis. (**A**) Specificity of *Dec1* and *Dec2* transcription for adult β cells in humans, pigs, and rodents, compared to known adult-restricted transcription factors regulating human β-cell functional maturation. Data are mean ±SEM from N =2-3 humans, 2-11 pigs, 3 rats, and 1-3 mice. (**B**) Oscillation of *Dec1* and *Dec2* transcripts in β-cells isolated every 4h for a day. Data are mean ±SEM of n =2 replicate measurements, each pooling N =6 mice. (**C**) Fasting blood glucose in *Dec1*$^{-/-}$ and *Dec2*$^{-/-}$ 2-3-month-old mice at ZT2. Data are pooled from N =31-35 (*Dec1*$^{+/+}$, *Dec1*$^{-/-}$) and 7 (*Dec2*$^{+/+}$, *Dec2*$^{-/-}$) mice. (**D**) Glucose tolerance in *Dec1*$^{-/-}$ and *Dec2*$^{-/-}$ 2-3-month-old mice following intraperitoneal glucose administration at ZT2. Data are mean ±SEM from N =34 WT, 41 *Dec1*$^{-/-}$, and 10 *Dec2*$^{-/-}$ mice. (**E**) Glucose-stimulated insulin secretion in *Dec1*$^{-/-}$ and *Dec2*$^{-/-}$ 8-month-old mice following intraperitoneal glucose administration at ZT2. Data are pooled from N =18 WT, 20 *Dec1*$^{-/-}$, and 3 *Dec2*$^{-/-}$ mice. *p <0.05, **p <0.01, ***p <0.001, t test [(C) and (D)] and Wilcoxon test (E).

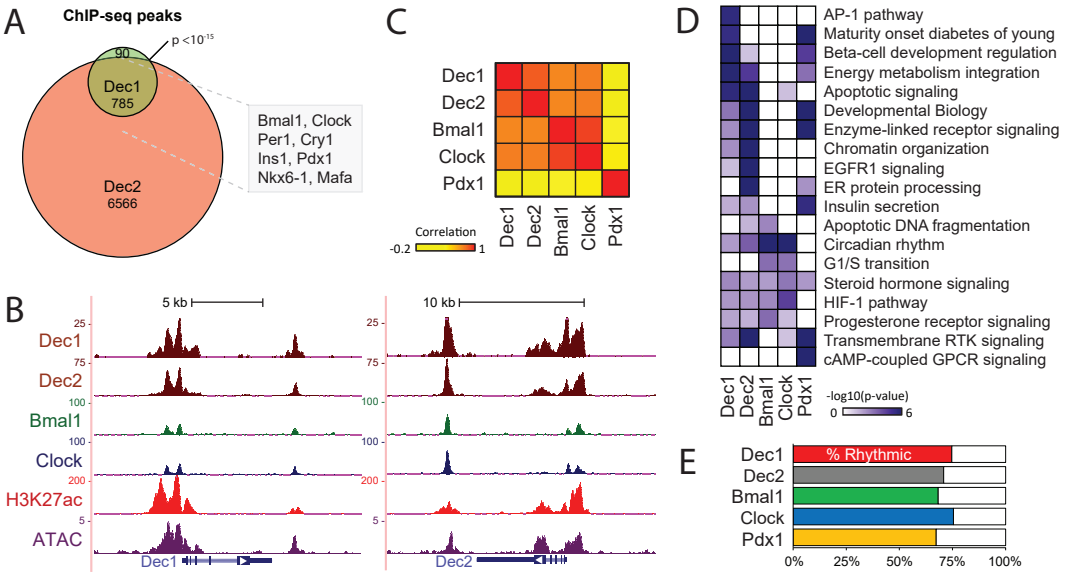

Fig. 2. Rhythmic energy metabolism and secretory genes are selectively bound by circadian clock DEC components. (**A**) Overlap between DEC1 and DEC2 binding peaks identified by ChIP-seq in β-cells, highlighting shared sites mapping to genes regulating circadian clock and β-cell function. (**B**) Genomic view of DEC1, DEC2, BMAL1, and CLOCK binding at *Dec1* and *Dec2* loci in β-cells. Tracks display normalized ChIP and ATAC sequencing read density. Gene models are shown below. (**C**) Correlation between DEC1, DEC2, BMAL1, CLOCK, and PDX1 ChIP-seq signal, calculated across the union of their respective binding peaks. (**D**) Pathways enriched among genes linked to binding peaks for DEC1, DEC2, BMAL1, CLOCK, and PDX1 in β-cells. (**E**) Fraction of DEC1, DEC2, BMAL1, CLOCK, and PDX1 target genes expressed rhythmically in β-cells.

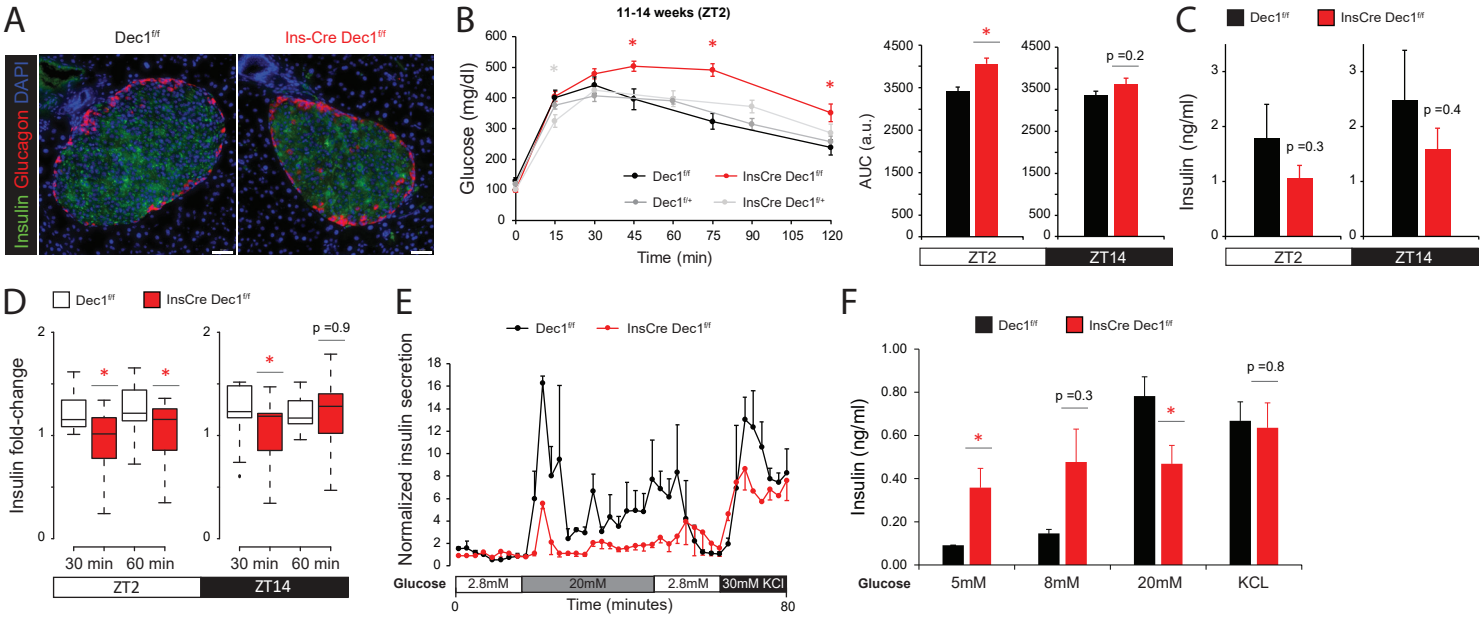

Fig. 3. β-cell DEC1 disruption causes glucose intolerance and hypoinsulinemia due to immature islet function. (**A**) Immunofluorescence staining of insulin (green), glucagon (red), and DAPI (blue) in *InsCre Dec1$^{f/f}$* and control mice pancreata. (**B**) Glucose tolerance in *InsCre Dec1$^{f/f}$* 3-month-old mice following intraperitoneal glucose administration at ZT2 (left, middle) and ZT14 (right). Data are mean ±SEM from N =20 *InsCre Dec1$^{f/f}$*, 17 *Dec1$^{f/f}$*, 12 *InsCre Dec1$^{f/+}$*, and 9 *Dec1$^{f/+}$* mice. (**C**) Blood insulin in *ad libitum* fed *InsCre Dec1$^{f/f}$* 2-3-month-old mice at ZT2 and ZT14. Data are mean ±SEM from N =15 *InsCre Dec1$^{f/f}$* and 11 *Dec1$^{f/f}$* mice with n =2 replicate measurements each. (**D**) Blood insulin secretion in *InsCre Dec1$^{f/f}$* 2-3-month-old mice following intraperitoneal glucose administration at ZT2 (left) and ZT14 (right). Data are pooled from N =14 *InsCre Dec1$^{f/f}$* and 10 *Dec1$^{f/f}$* mice. (**E**) Glucose-stimulated insulin secretion dynamics in perifused *InsCre Dec1$^{f/f}$* islets. Data are mean ±SEM from N =2 *InsCre Dec1$^{f/f}$* and 2 *Dec1$^{f/f}$* mice, each with n =2-4 replicate measurements of 20 similar-sized islets, normalized to the mean of the first incubation. (**F**) Insulin secretion from isolated *InsCre Dec1$^{f/f}$* islets at increasing glucose concentrations. Data are mean ±SEM from N =10 *InsCre Dec1$^{f/f}$* and 9 *Dec1$^{f/f}$* mice, each with n =2 replicate measurements of 20 size-matched islets. *p <0.05, t test.

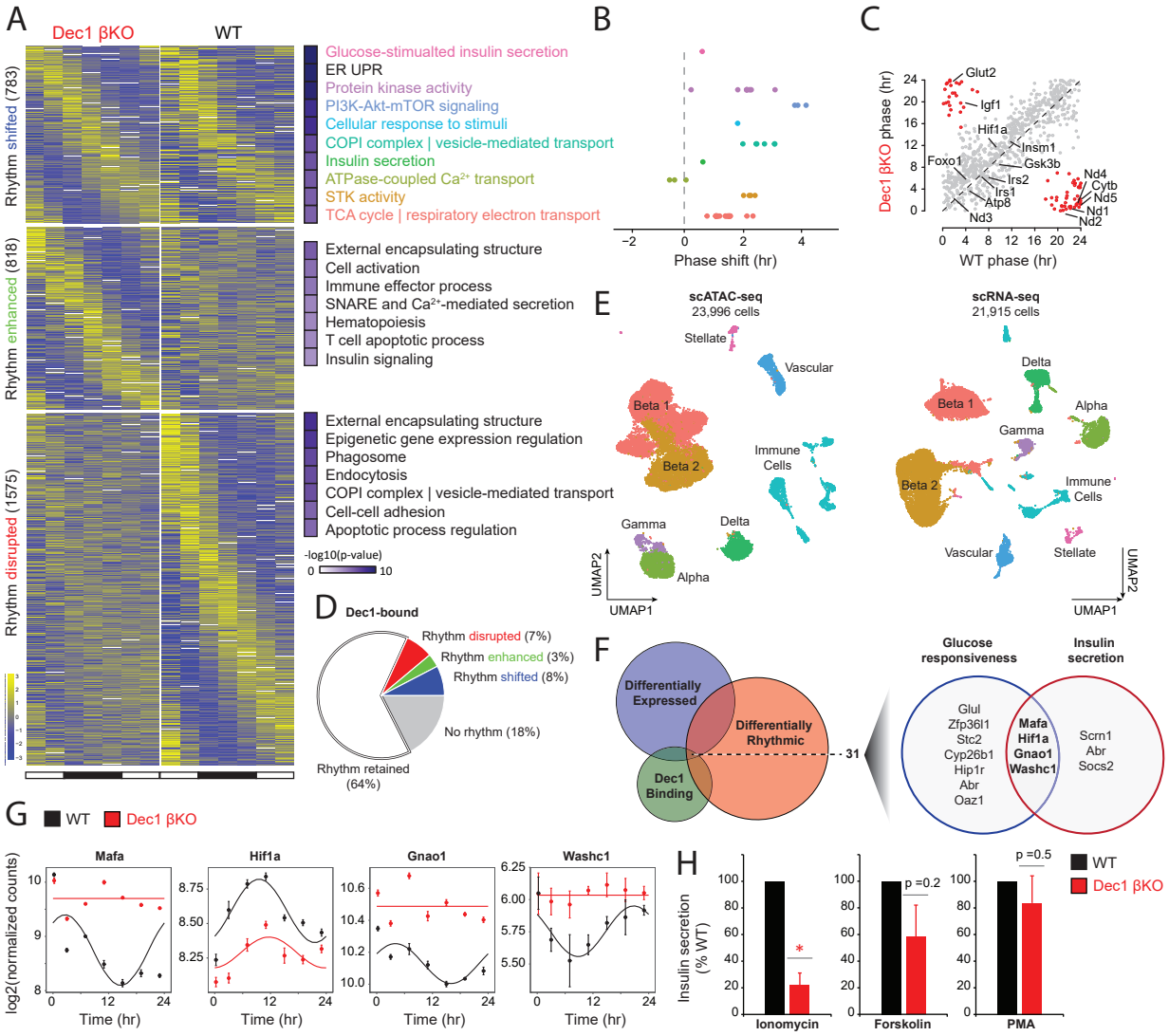

Fig. 4. DEC1 synchronizes respiratory metabolism and insulin secretion gene rhythms in pancreatic β-cells. (**A-B**) Expression of rhythm disrupted (bottom), enhanced (middle), and shifted (top) transcripts in *Dec1*-βKO mice compared to littermate controls (A, left), highlighting pathways enriched among differentially rhythmic genes (A, right), and phase change for pathways enriched among genes whose expression rhythm is shifted in *Dec1*-βKO mice (B), colored by functional category. Data are mean from n =4 replicate measurements, each pooling N =2 mice. (**C**) Phase change for genes with shifted transcription rhythm in *Dec1*-βKO mice, highlighting mediators of glucose sensing, metabolism, and insulin secretion. (**D**) Fraction of DEC1-bound genes with noncyclic (gray) or cyclic expression that is retained (white), disrupted (red), enhanced (green) or shifted (blue) in *Dec1*-βKO mice. (**E**) Clustering of single-cell open chromatin profiles, assayed by ATAC sequencing (right), and gene expression profiles, assayed by RNA sequencing (left), from isolated *Dec1*-βKO and littermate control islets. Data are pooled from N =2 WT and 2 *Dec1*-βKO mice, each sequenced separately. (**F**) Overlap between DEC1 targets in β cells and genes that are differentially rhythmic and differentially expressed in β cells from *Dec1*-βKO mice compared to littermate controls, highlighting the significant enrichment in shared genes mediating glucose responsiveness and insulin secretion. (**G**) Temporal expression pattern of *Mafa, Hif1a, Gnao1*, and *Washc1* in *Dec1*-βKO mice and littermate controls. Data are mean from n =4 replicate measurements, each pooling N =2 mice. (**H**) Glucose- and secretagogue-stimulated insulin secretion in size-matched islets isolated from *Dec1*-βKO mice and littermate controls. Data are mean ±SEM from N = 6 WT and 5 *Dec1*-βKO mice, each with n =2-3 replicate measurements, normalized to intracellular insulin content.

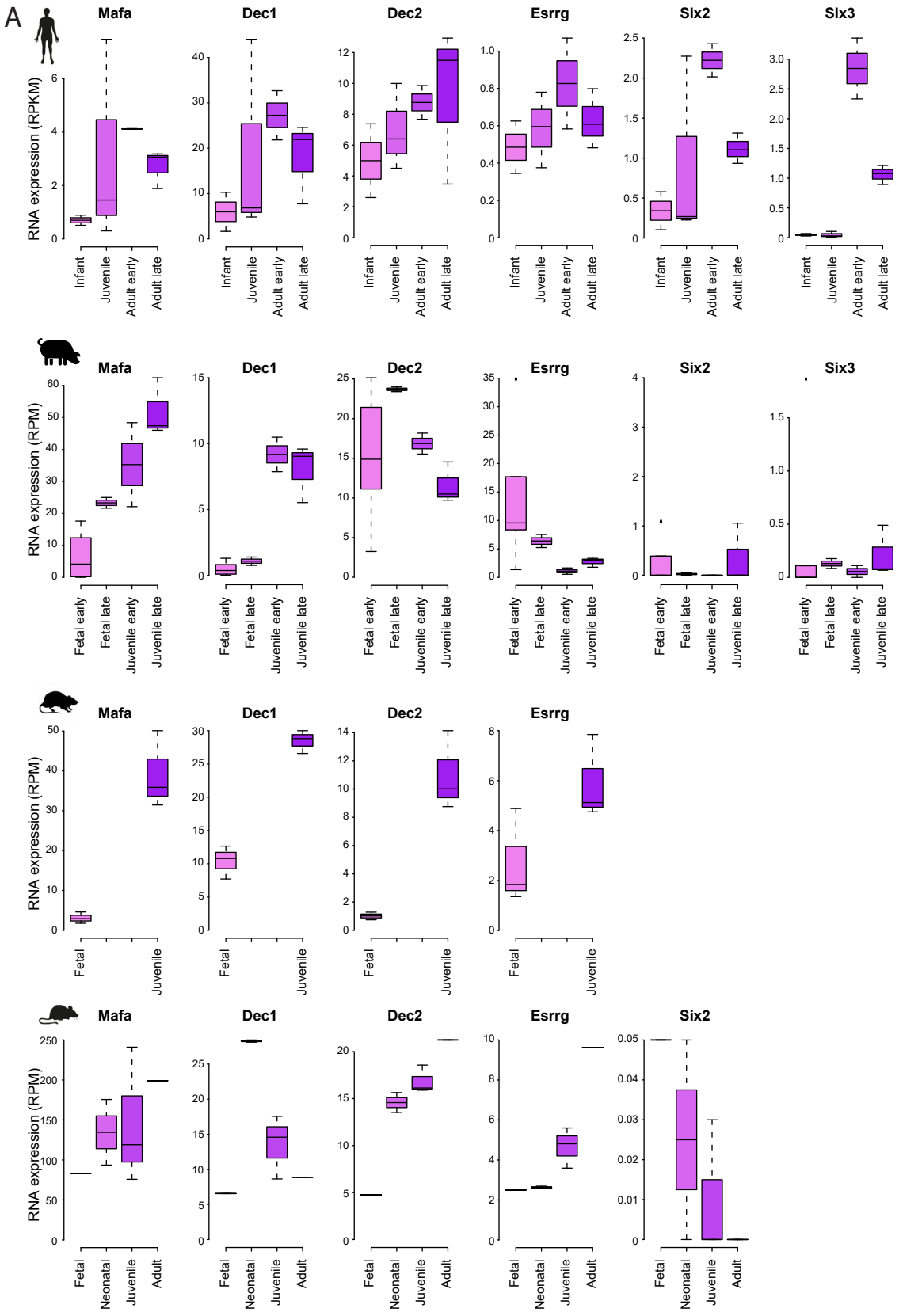
A
Mafa
Dec1
Dec2
Esrrg
Six2
Six3
RNA expression (RPKM)
Infant
Juvenile
Adult early
Adult late
RNA expression (RPM)
Fetal early
Fetal late
Juvenile early
Juvenile late
Fetal
Neonatal
Adult

Fig. S1. Circadian clock DEC components mark mature β cells across species.

Specificity of *Dec1* and *Dec2* RNA expression for adult β cells in humans, pigs, and rodents, compared to known adult-restricted transcription factors regulating human β-cell functional maturation. Data are pooled from N =2-3 humans, 2-11 pigs, 3 rats, and 1-3 mice at each stage.

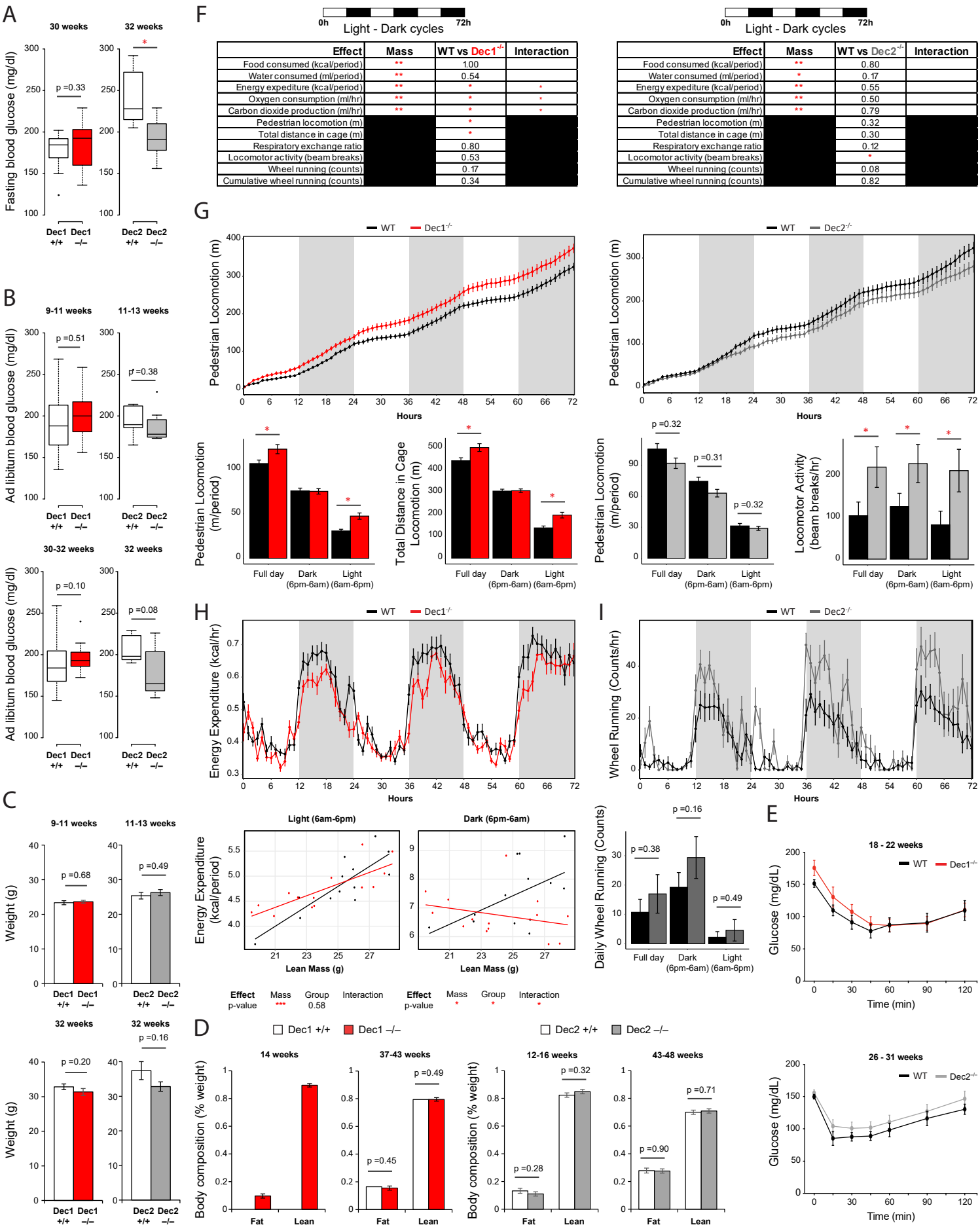
A
30 weeks
32 weeks
Fasting blood glucose (mg/dl)
p =0.33
*
Dec1 +/+
Dec1 –/–
Dec2 +/+
Dec2 –/–
B
9-11 weeks
11-13 weeks
Ad libitum blood glucose (mg/dl)
p =0.51
p =0.38
30-32 weeks
32 weeks
p =0.10
p =0.08
C
9-11 weeks
11-13 weeks
Weight (g)
p =0.68
p =0.49
32 weeks
32 weeks
p =0.20
p =0.16
F
0h
72h
Light - Dark cycles
Effect | Mass | WT vs Dec1-/- | Interaction
Food consumed (kcal/period) | ** | 1.00
Water consumed (ml/period) | ** | 0.54
Energy expediture (kcal/period) | ** | * | *
Oxygen consumption (ml/hr) | ** | * | *
Carbon dioxide production (ml/hr) | ** | * | *
Pedestrian locomotion (m) | | *
Total distance in cage (m) | | *
Respiratory exchange ratio | | 0.80
Locomotor activity (beam breaks) | | 0.53
Wheel running (counts) | | 0.17
Cumulative wheel running (counts) | | 0.34
Effect | Mass | WT vs Dec2-/- | Interaction
Food consumed (kcal/period) | ** | 0.80
Water consumed (ml/period) | * | 0.17
Energy expediture (kcal/period) | ** | 0.55
Oxygen consumption (ml/hr) | ** | 0.50
Carbon dioxide production (ml/hr) | ** | 0.79
Pedestrian locomotion (m) | | 0.32
Total distance in cage (m) | | 0.30
Respiratory exchange ratio | | 0.12
Locomotor activity (beam breaks) | | *
Wheel running (counts) | | 0.08
Cumulative wheel running (counts) | | 0.82
G
WT
Dec1-/-
Dec2-/-
Pedestrian Locomotion (m)
Hours
Pedestrian Locomotion (m/period)
Total Distance in Cage Locomotion (m)
Locomotor Activity (beam breaks/hr)
Full day
Dark (6pm-6am)
Light (6am-6pm)
p =0.32
p =0.31
H
Energy Expenditure (kcal/hr)
Light (6am-6pm)
Dark (6pm-6am)
Energy Expenditure (kcal/period)
Lean Mass (g)
Effect | Mass | Group | Interaction
p-value | *** | 0.58
Effect | Mass | Group | Interaction
p-value | * | * | *
I
Wheel Running (Counts/hr)
Daily Wheel Running (Counts)
p =0.16
p =0.38
p =0.49
E
18 - 22 weeks
Glucose (mg/dL)
Time (min)
D
Dec1 +/+
Dec1 –/–
Dec2 +/+
Dec2 –/–
14 weeks
37-43 weeks
12-16 weeks
43-48 weeks
Body composition (% weight)
Fat
Lean
p =0.45
p =0.49
p =0.28
p =0.32
p =0.90
p =0.71
26 - 31 weeks

J

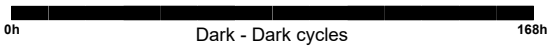

Effect	Mass	WT vs Dec1$^{-/-}$	Interaction
Food consumed (kcal/period)	0.11	0.78	
Water consumed (ml/period)	0.55	0.76	
Energy expediture (kcal/period)	**	*	*
Oxygen consumption (ml/hr)	**	*	*
Carbon dioxide production (ml/hr)	**	*	*
Pedestrian locomotion (m)		**	
Total distance in cage (m)		**	
Respiratory exchange ratio		0.98	
Locomotor activity (beam breaks)		0.43	
Wheel running (counts)		0.38	
Cumulative wheel running (counts)		0.72	

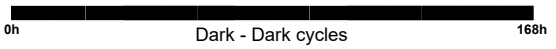

Effect	Mass	WT vs Dec2$^{-/-}$	Interaction
Food consumed (kcal/period)	*	0.50	
Water consumed (ml/period)	**	0.17	
Energy expediture (kcal/period)	*	0.88	
Oxygen consumption (ml/hr)	*	0.89	
Carbon dioxide production (ml/hr)	**	0.86	
Pedestrian locomotion (m)		*	
Total distance in cage (m)		0.70	
Respiratory exchange ratio		0.40	
Locomotor activity (beam breaks)		0.09	
Wheel running (counts)		*	
Cumulative wheel running (counts)		0.45	

Q

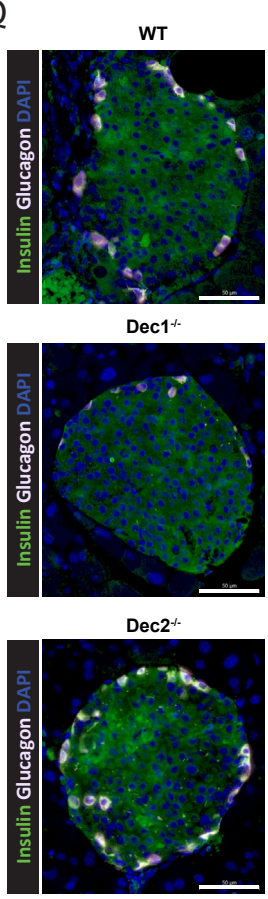

K

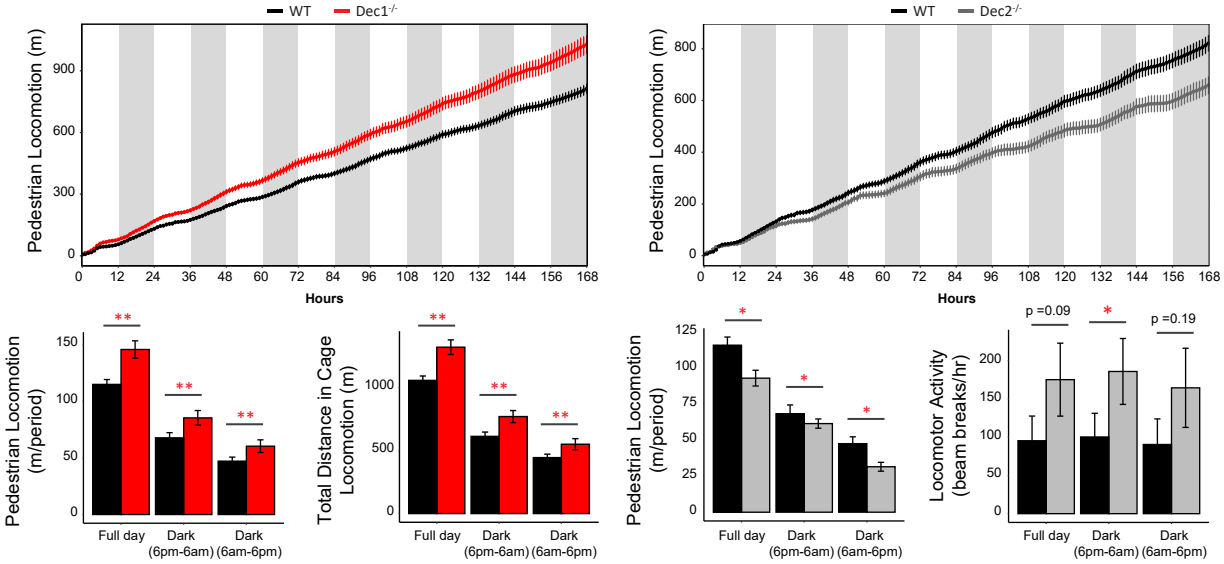

L

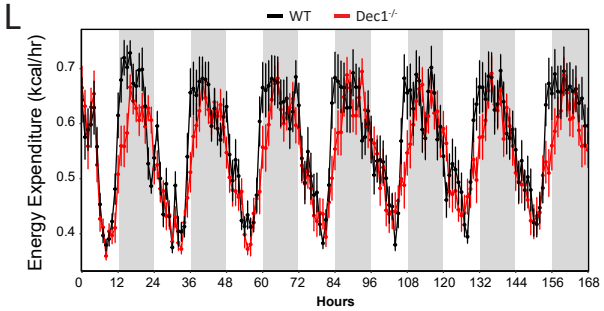

Effect p-value	Mass	Group	Interaction
	**	0.52	

Effect p-value	Mass	Group	Interaction
	**	*	*

M

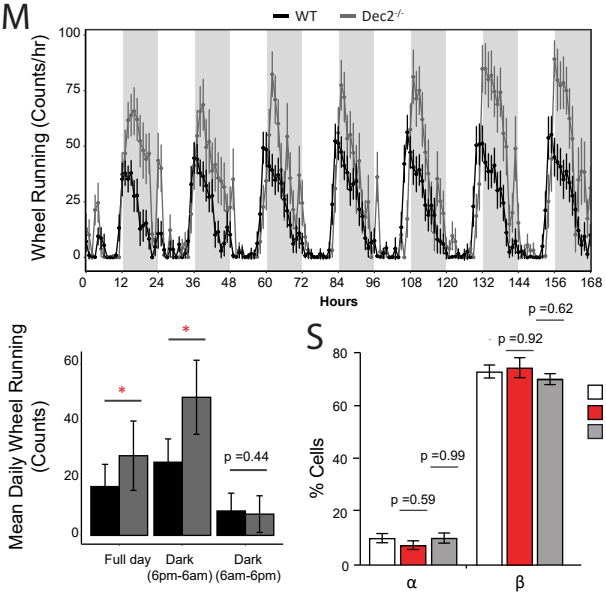

R

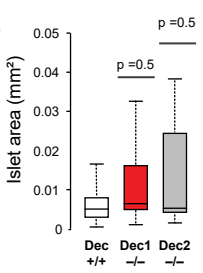

S

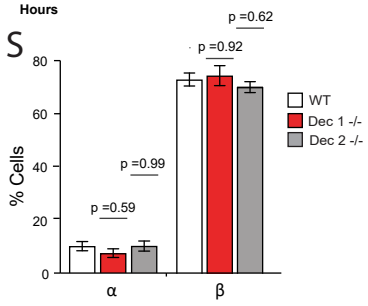

T

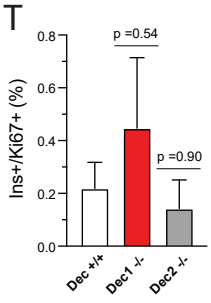

N

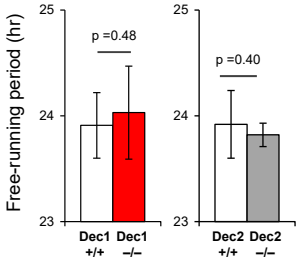

O

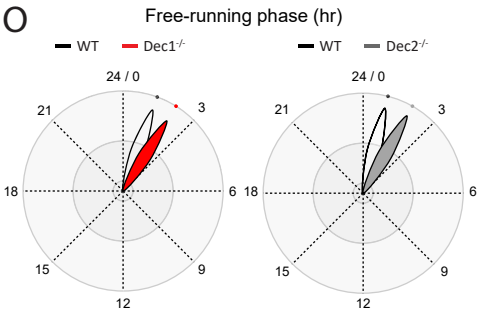

P

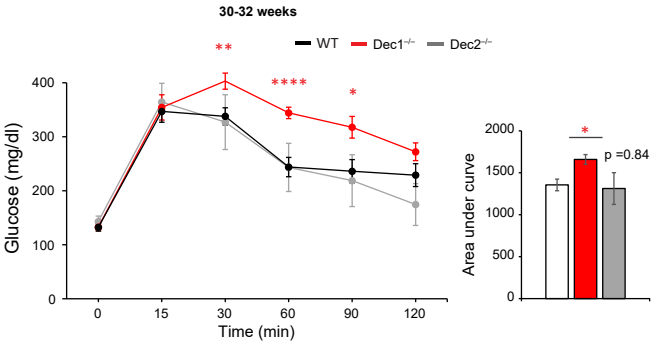

Fig. S2. Elevated blood glucose, hypometabolism, and glucose intolerance in young and aged *Dec1*-disrupted mice despite normal food intake, insulin sensitivity, and islet formation.

(**A**) Fasting blood glucose in *Dec1*$^{-/-}$ and *Dec2*$^{-/-}$ 8-month-old mice at ZT2. Data are pooled from N =16-18 (*Dec1*$^{+/+}$, *Dec1*$^{-/-}$) and 5-7 (*Dec2*$^{+/+}$, *Dec2*$^{-/-}$) mice.

(**B**) Blood glucose in ad libitum fed *Dec1*$^{-/-}$ and *Dec2*$^{-/-}$ 2-3-month-old (N =13 *Dec1*$^{-/-}$, 7 *Dec2*$^{-/-}$, and 19 littermate control) and 8-month-old (N =21 *Dec1*$^{-/-}$, 7 *Dec2*$^{-/-}$, and 39 littermate control) mice at ZT2.

(**C**) Weight of *Dec1*$^{-/-}$ and *Dec2*$^{-/-}$ 2-3-month-old (N =38 *Dec1*$^{-/-}$, 11 *Dec2*$^{-/-}$, and 42 littermate control) and 8-month-old (N =25 *Dec1*$^{-/-}$, 7 *Dec2*$^{-/-}$, and 11 littermate control) mice at ZT2. Data are mean ±SEM.

(**D**) Body composition of *Dec1*$^{-/-}$ and *Dec2*$^{-/-}$ 3-4-month-old (N =7 *Dec1*$^{-/-}$, 5 *Dec2*$^{-/-}$, and 12 littermate control) and aged (N =5 *Dec1*$^{-/-}$, 2 *Dec2*$^{-/-}$, and 9 littermate control) mice.

(**E**) Insulin tolerance in 4-5-month-old *Dec1*$^{-/-}$ and 6-7-month-old *Dec2*$^{-/-}$ mice following intraperitoneal insulin administration at ZT2. Data are mean ±SEM from N =7 *Dec1*$^{-/-}$, 10 *Dec2*$^{-/-}$, and 17 littermate control mice.

(**F**) Summary of results from indirect calorimetry experiments for 14 *Dec1*$^{-/-}$ (left), 4 *Dec2*$^{-/-}$ (right), and 13 littermate control mice across 3 days in 12-hour light-dark cycles. Shown are p-values corresponding to model coefficients for group effects, along with the mass and interaction effects for mass-dependent measurements.

(**G**) Top: cumulative pedestrian locomotion of 14 *Dec1*$^{-/-}$ (left), 4 *Dec2*$^{-/-}$ (right), and 13 littermate control mice across 3 days in 12-hour light-dark cycles. Bottom: overall daily values by group and photoperiod for pedestrian locomotion, total distance in cage, and locomotor activity measurements. Data are mean ±SEM.

(**H**) Top: daily energy expenditure rhythms of 14 *Dec1*$^{-/-}$ mice across 3 days in 12-hour light-dark cycles. Data are mean ±SEM. Bottom: regression analysis for energy expenditure and lean body mass by photoperiod. Model coefficients for mass, group, and interaction effects are indicated below.

(**I**) Top: daily wheel running rhythms of 4 *Dec2*$^{-/-}$ mice across 3 days in 12-hour light-dark cycles. Data are mean ±SEM. Bottom: overall daily values by group and photoperiod.

(**J**) Summary of results from indirect calorimetry experiments of 14 *Dec1*$^{-/-}$ (left), 4 *Dec2*$^{-/-}$ (right), and 13 littermate control mice across 7 days in 12-hour dark-dark cycles. Shown are p-values corresponding to model coefficients for genotype effects, along with the mass and interaction effects for mass-dependent measurements.

(**K**) Top: cumulative pedestrian locomotion of 14 *Dec1*$^{-/-}$ (left), 4 *Dec2*$^{-/-}$ (right), and 13 littermate control mice across 7 days in 12-hour dark-dark cycles. Bottom: overall daily mean

values by group and photoperiod for pedestrian locomotion, total distance in cage, and locomotor activity measurements. Data are mean ±SEM.

(**L**) Top: daily energy expenditure rhythms of 14 *Dec1*$^{-/-}$ mice across 7 days in 12-hour dark-dark cycles. Data are mean ±SEM. Bottom: regression analysis for energy expenditure and lean body mass by photoperiod. Model coefficients for mass, group, and interaction effects are indicated below.

(**M**) Top: daily wheel running rhythms of 4 *Dec2*$^{-/-}$ mice across 7 days in 12-hour dark-dark cycles. Data are mean ±SEM. Bottom: overall daily values by group and photoperiod.

(**N-O**) Free-running period (N) and phase (O) of wheel running rhythms of 14 *Dec1*$^{-/-}$ (left), 4 *Dec2*$^{-/-}$ (right), and 13 littermate control mice across 7 days in 12-hour dark-dark cycles.

(**P**) Glucose tolerance in *Dec1*$^{-/-}$ and *Dec2*$^{-/-}$ 8-month-old mice following intraperitoneal glucose administration at ZT2. Data are mean ±SEM from N =22 *Dec1*$^{-/-}$, 7 *Dec2*$^{-/-}$, and 8 WT mice.

(**Q**) Immunofluorescence staining of insulin (green), glucagon (magenta), and DAPI (blue) in *Dec1*$^{-/-}$, *Dec2*$^{-/-}$, and control mice pancreata.

(**R**) Islet area in *Dec1*$^{-/-}$, *Dec2*$^{-/-}$, and control mice pancreata. Data are mean ±SEM from n = islets pooled from N =1-2 mice.

(**S**) Proportion of islet alpha and beta cells in *Dec1*$^{-/-}$, *Dec2*$^{-/-}$, and control mice pancreata. Data are pooled from N =1-2 mice.

(**T**) Fraction of proliferating (Ki67+) beta cells in *Dec1*$^{-/-}$, *Dec2*$^{-/-}$, and control mice pancreata. Data are pooled from N =1-2 mice.

*p <0.05, **p <0.01, ***p <0.001, ****p <0.0001, t test [(A-E) and (N-T)], ANOVA [(G), (I), (K), and (M)], and ANCOVA [(H) and (L)].

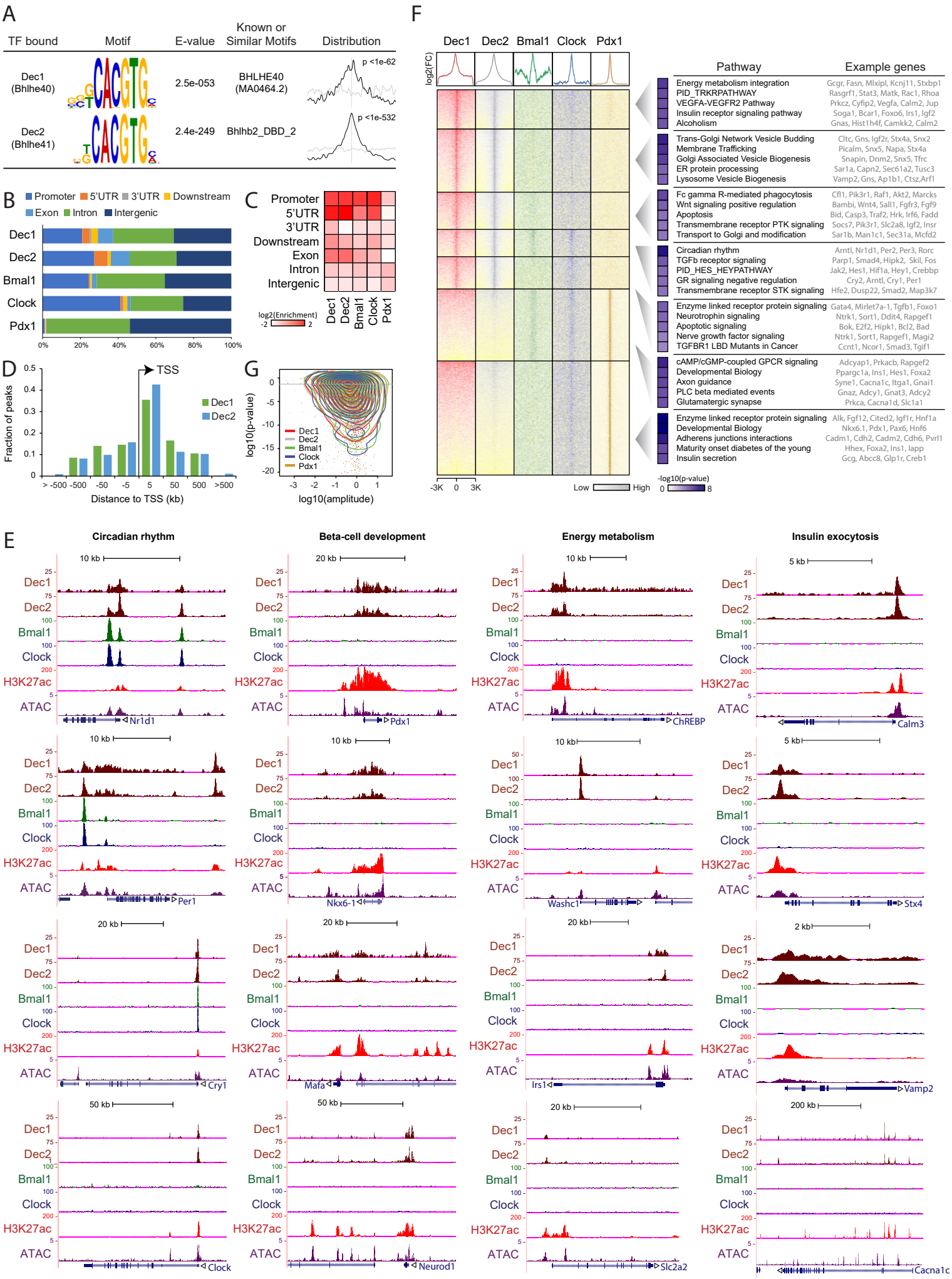
A
TF bound
Motif
E-value
Known or Similar Motifs
Distribution
Dec1 (Bhlhe40)
2.5e-053
BHLHE40 (MA0464.2)
p <1e-62
Dec2 (Bhlhe41)
2.4e-249
Bhlhb2_DBD_2
p <1e-532
B
Promoter
5'UTR
3'UTR
Downstream
Exon
Intron
Intergenic
Dec1
Dec2
Bmal1
Clock
Pdx1
0%
20%
40%
60%
80%
100%
C
log2(Enrichment)
-2
2
D
TSS
Fraction of peaks
Distance to TSS (kb)
> -500
-500
-50
-5
5
50
500
>500
G
log10(p-value)
log10(amplitude)
F
Dec1
Dec2
Bmal1
Clock
Pdx1
log2(FC)
-3K
0
3K
Low
High
-log10(p-value)
Pathway
Example genes
Energy metabolism integration
Gcgr, Fasn, Mlxipl, Kcnj11, Stxbp1
PID_TRKRPATHWAY
Rasgrf1, Stat3, Matk, Rac1, Rhoa
VEGFA-VEGFR2 Pathway
Prkcz, Cyfip2, Vegfa, Calm2, Jup
Insulin receptor signaling pathway
Soga1, Bcar1, Foxo6, Irs1, Igf2
Alcoholism
Gnas, Hist1h4f, Camkk2, Calm2
Trans-Golgi Network Vesicle Budding
Cltc, Gns, Igf2r, Stx4a, Snx2
Membrane Trafficking
Picalm, Snx5, Napa, Stx4a
Golgi Associated Vesicle Biogenesis
Snapin, Dnm2, Snx5, Tfrc
ER protein processing
Sar1a, Capn2, Sec61a2, Tusc3
Lysosome Vesicle Biogenesis
Vamp2, Gns, Ap1b1, Ctsz,Arf1
Fc gamma R-mediated phagocytosis
Cfl1, Pik3r1, Raf1, Akt2, Marcks
Wnt signaling positive regulation
Bambi, Wnt4, Sall1, Fgfr3, Fgf9
Apoptosis
Bid, Casp3, Traf2, Hrk, Irf6, Fadd
Transmembrane receptor PTK signaling
Socs7, Pik3r1, Slc2a8, Igf2, Insr
Transport to Golgi and modification
Sar1b, Man1c1, Sec31a, Mcfd2
Circadian rhythm
Arntl, Nr1d1, Per2, Per3, Rorc
TGFb receptor signaling
Parp1, Smad4, Hipk2, Ski, Fos
PID_HES_HEYPATHWAY
Jak2, Hes1, Hif1a, Hey1, Crebbp
GR signaling negative regulation
Cry2, Arntl, Cry1, Per1
Transmembrane receptor STK signaling
Hfe2, Dusp22, Smad2, Map3k7
Enzyme linked receptor protein signaling
Gata4, Mirlet7a-1, Tgfb1, Foxo1
Neurotrophin signaling
Ntrk1, Sort1, Ddit4, Rapgef1
Apoptotic signaling
Bok, E2f2, Hipk1, Bcl2, Bad
Nerve growth factor signaling
Ntrk1, Sort1, Rapgef1, Magi2
TGFBR1 LBD Mutants in Cancer
Ccnt1, Ncor1, Smad3, Tgif1
cAMP/cGMP-coupled GPCR signaling
Adcyap1, Prkacb, Rapgef2
Developmental Biology
Ppargc1a, Ins1, Hes1, Foxa2
Axon guidance
Syne1, Cacna1c, Itga1, Gnai1
PLC beta mediated events
Gnaz, Adcy1, Gnat3, Adcy2
Glutamatergic synapse
Prkca, Cacna1d, Slc1a1
Enzyme linked receptor protein signaling
Alk, Fgf12, Cited2, Igf1r, Hnf1a
Developmental Biology
Nkx6.1, Pdx1, Pax6, Hnf6
Adherens junctions interactions
Cadm1, Cdh2, Cadm2, Cdh6, Pvrl1
Maturity onset diabetes of the young
Hhex, Foxa2, Ins1, Iapp
Insulin secretion
Gcg, Abcc8, Glp1r, Creb1
E
Circadian rhythm
Beta-cell development
Energy metabolism
Insulin exocytosis
Dec1
Dec2
Bmal1
Clock
H3K27ac
ATAC
Nr1d1
Pdx1
ChREBP
Calm3
Per1
Nkx6-1
Washc1
Stx4
Cry1
Maf
Irs1
Vamp2
Clock
Neurod1
Slc2a2
Cacna1c

Fig. S3. Clock DEC components selectively bind to energy metabolism and insulin secretion genes.

(**A**) DEC1 and DEC2 binding peaks identified by ChIP-seq in β-cells enrich for the known DEC1 and DEC2 recognition motifs, respectively. Show are the top motif identified by MEME-ChIP (*52*) across peak regions, its significance (E-value), top known motif match, and the distribution of the best matches to the motif across center-aligned peak regions. on.

(**B**) Distribution of genomic locations for DEC1, DEC2, BMAL1, CLOCK, and PDX1 binding peaks from ChIP-seq in β-cells.

(**C**) Relative enrichment for genomic locations among DEC1, DEC2, BMAL1, CLOCK, and PDX1 binding peaks from ChIP-seq in β-cells.

(**D**) Distance to the nearest TSS for DEC1, DEC2, BMAL1, CLOCK, and PDX1 binding peaks from ChIP-seq in β-cells.

(**E**) Genomic view of DEC1, DEC2, BMAL1, and CLOCK binding in β-cells at genes regulating the circadian rhythm, beta-cell development, energy metabolism, and insulin excocytosis. Tracks display normalized ChIP and ATAC sequencing read density. Gene models are shown below.

(**F**) Left: density of ChIP-seq signal enrichment over input ±3kb around the center of each DEC1, DEC2, BMAL1, CLOCK, and PDX1 binding peak in β-cells. Right: pathways enriched among genes linked to binding peaks for DEC1, DEC2, BMAL1, CLOCK, and PDX1 in β-cells.

(**G**) Relationship between expression amplitude (peak-to-trough ratio), and significance of rhythmicity, as determined by dryR (*13*), for all genes linked to DEC1, DEC2, BMAL1, CLOCK, and PDX1 binding peaks from ChIP-seq in β-cells, indicating the $p < 0.05$ threshold used.

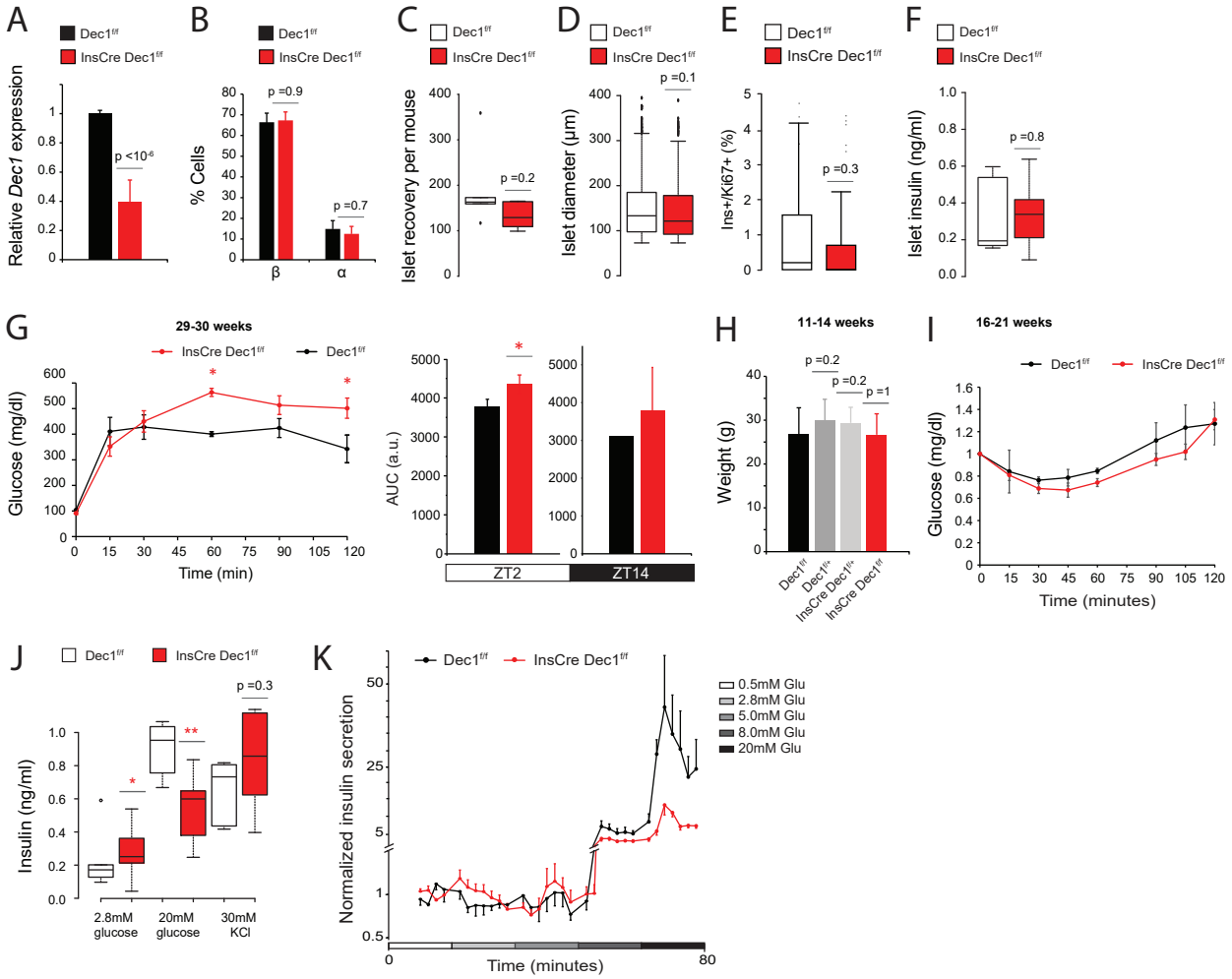
A
Dec1f/f
InsCre Dec1f/f
Relative Dec1 expression
p <10-6
B
% Cells
p =0.9
p =0.7
β
α
C
Islet recovery per mouse
p =0.2
D
Islet diameter (µm)
p =0.1
E
Ins+/Ki67+ (%)
p =0.3
F
Islet insulin (ng/ml)
p =0.8
G
29-30 weeks
Glucose (mg/dl)
Time (min)
AUC (a.u.)
ZT2
ZT14
H
11-14 weeks
Weight (g)
p =0.2
p =0.2
p =1
I
16-21 weeks
Glucose (mg/dl)
Time (minutes)
J
Insulin (ng/ml)
p =0.3
2.8mM glucose
20mM glucose
30mM KCl
K
Normalized insulin secretion
Time (minutes)
0.5mM Glu
2.8mM Glu
5.0mM Glu
8.0mM Glu
20mM Glu

Fig. S4. Glucose intolerance and immature islet function in young and aged β-cell specific *Dec1*-mutant mice despite normal weight, insulin sensitivity, and islet formation.

(**A**) Relative *Dec1* mRNA expression in isolated *InsCre Dec1*$^{f/f}$ islets. Data are mean from n =4 replicate measurements, each pooling N =2 *InsCre Dec1*$^{f/f}$ and 2 *Dec1*$^{f/f}$ mice.

(**B**) Proportion of islet alpha and beta cells in isolated *InsCre Dec1*$^{f/f}$ islets. Data are pooled from N =2 *InsCre Dec1*$^{f/f}$ and 3 *Dec1*$^{f/f}$ mice.

(**C**) Islets isolated for each of 5 *InsCre Dec1*$^{f/f}$ and 5 *Dec1*$^{f/f}$ mice.

(**D**) Diameter of isolated *InsCre Dec1*$^{f/f}$ islets. Data are pooled from N =5 *InsCre Dec1*$^{f/f}$ and 5 *Dec1*$^{f/f}$ mice.

(**E**) Fraction of proliferating (Ki67+) beta cells in *InsCre Dec1*$^{f/f}$ and *Dec1*$^{f/f}$ mice pancreata. Data are pooled from N =1-2 mice.

(**F**) Insulin content of isolated *InsCre Dec1*$^{f/f}$ islets. Data are pooled from N =6 *InsCre Dec1*$^{f/f}$ and 6 *Dec1*$^{f/f}$ mice.

(**G**) Glucose tolerance in *InsCre Dec1*$^{f/f}$ 8-month-old mice following intraperitoneal glucose administration at ZT2. Data are mean ±SEM from N =20 *InsCre Dec1*$^{f/f}$ and 17 *Dec1*$^{f/f}$ mice.

(**H**) Weight of 20 *InsCre Dec1*$^{f/f}$, 17 *Dec1*$^{f/f}$, 12 *InsCre Dec1*$^{f/+}$, and 9 *Dec1*$^{f/+}$ 2-3-month-old mice at ZT2. Data are mean ±SEM.

(**I**) Insulin tolerance in *InsCre Dec1*$^{f/f}$ 4-5-month-old mice following intraperitoneal insulin administration at ZT2. Data are mean ±SEM from N =3 *InsCre Dec1*$^{f/f}$ and 3 *Dec1*$^{f/f}$ mice.

(**J**) Glucose-stimulated insulin secretion of isolated *InsCre Dec1*$^{f/f}$ islets. Data are pooled from N =6 *InsCre Dec1*$^{f/f}$ and 6 *Dec1*$^{f/f}$ mice.

(**K**) Insulin secretion dynamics in perifused *InsCre Dec1*$^{f/f}$ islets across a glucose ramp. Data are mean ±SEM from N =2 *InsCre Dec1*$^{f/f}$ and 2 *Dec1*$^{f/f}$ mice, each with n =3 replicate measurements of 20 size-matched islets, normalized to the mean of the first incubation.

*$p < 0.05$, t test.

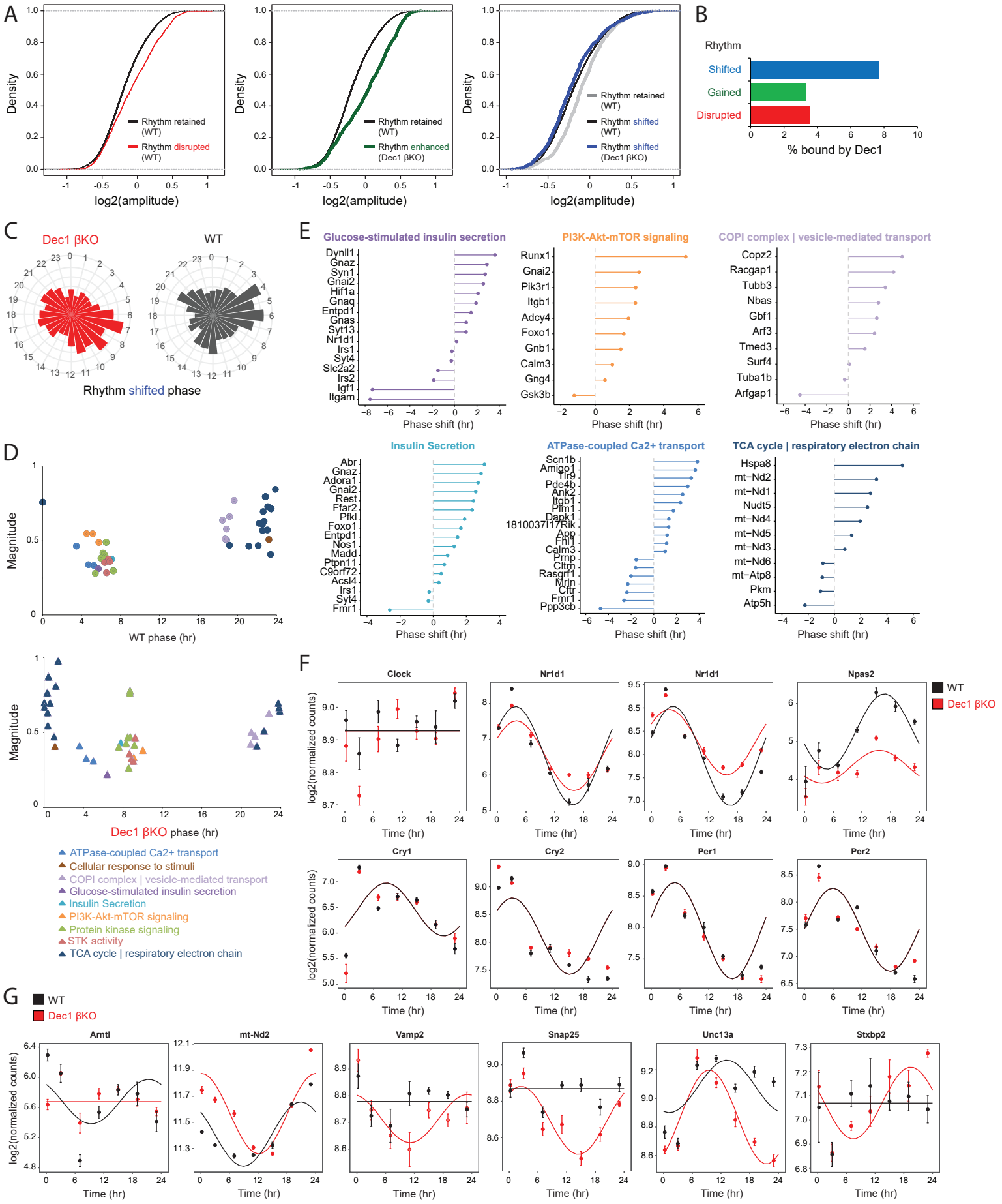
A
Density
log2(amplitude)
Rhythm retained (WT)
Rhythm disrupted (WT)
Rhythm enhanced (Dec1 βKO)
Rhythm shifted (WT)
Rhythm shifted (Dec1 βKO)
B
Rhythm
Shifted
Gained
Disrupted
% bound by Dec1
C
Dec1 βKO
WT
Rhythm shifted phase
D
Magnitude
WT phase (hr)
Dec1 βKO phase (hr)
ATPase-coupled Ca2+ transport
Cellular response to stimuli
COPI complex | vesicle-mediated transport
Glucose-stimulated insulin secretion
Insulin Secretion
PI3K-Akt-mTOR signaling
Protein kinase signaling
STK activity
TCA cycle | respiratory electron chain
E
Glucose-stimulated insulin secretion
PI3K-Akt-mTOR signaling
COPI complex | vesicle-mediated transport
Insulin Secretion
ATPase-coupled Ca2+ transport
TCA cycle | respiratory electron chain
Phase shift (hr)
F
Clock
Nr1d1
Nr1d1
Npas2
Cry1
Cry2
Per1
Per2
log2(normalized counts)
Time (hr)
WT
Dec1 βKO
G
WT
Dec1 βKO
Arntl
mt-Nd2
Vamp2
Snap25
Unc13a
Stxbp2
log2(normalized counts)
Time (hr)

Fig. S5. Dec1 coordinates β-cell respiratory metabolism and insulin secretion gene rhythms.

(**A**) Cumulative density of oscillation amplitudes for genes whose expression rhythm is disrupted (left), enhanced (middle), and shifted (right) in Dec1 βKO mice, compared to those of rhythm retaining genes.

(**B**) Proportion of genes whose expression rhythm is disrupted, enhanced, or shifted in Dec1 βKO mice that is bound by DEC1 in β cells.

(**C**) Phase distribution of transcripts whose cyclic expression is shifted in Dec1 βKO mice.

(**D**) Magnitude and phase of enriched pathways among genes whose expression rhythm is shifted in Dec1 βKO mice, colored by biological theme.

(**E**) Phase change for genes whose cyclic expression is shifted in Dec1 βKO mice, grouped and colored by biological theme.

(**F-G**) Examples of genes with unaltered (F) and altered (G) temporal expression patterns in *Dec1*-βKO mice and littermate controls. Data are mean from n =4 replicate measurements, each pooling N =2 mice.

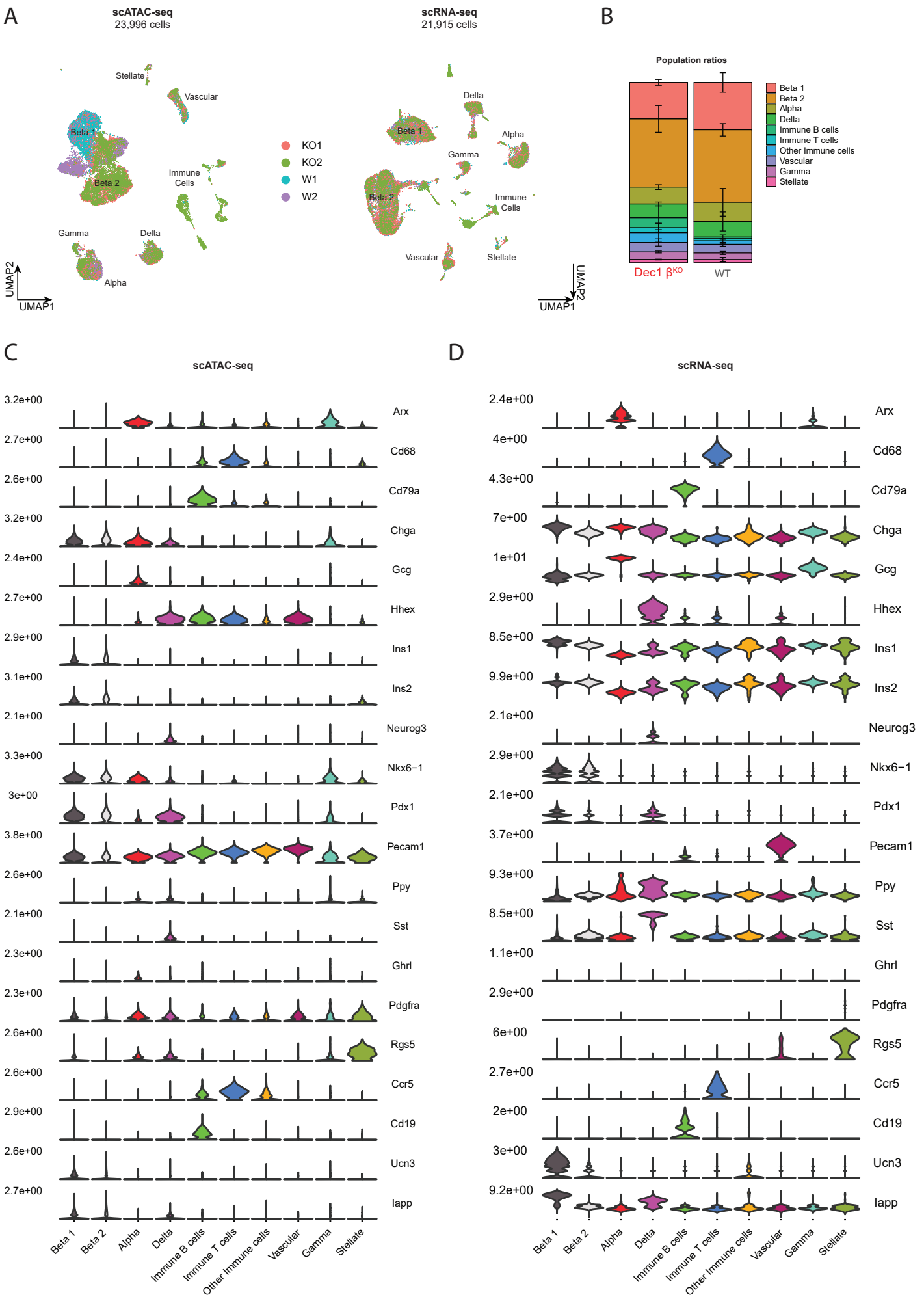
A
scATAC-seq
23,996 cells
Stellate
Vascular
Beta 1
Beta 2
Immune Cells
Gamma
Delta
Alpha
UMAP2
UMAP1
KO1
KO2
W1
W2
scRNA-seq
21,915 cells
Delta
Beta 1
Alpha
Gamma
Beta 2
Immune Cells
Vascular
Stellate
UMAP2
UMAP1
B
Population ratios
Beta 1
Beta 2
Alpha
Delta
Immune B cells
Immune T cells
Other Immune cells
Vascular
Gamma
Stellate
Dec1 βKO
WT
C
scATAC-seq
Arx
Cd68
Cd79a
Chga
Gcg
Hhex
Ins1
Ins2
Neurog3
Nkx6−1
Pdx1
Pecam1
Ppy
Sst
Ghrl
Pdgfra
Rgs5
Ccr5
Cd19
Ucn3
Iapp
Beta 1
Beta 2
Alpha
Delta
Immune B cells
Immune T cells
Other Immune cells
Vascular
Gamma
Stellate
D
scRNA-seq
Arx
Cd68
Cd79a
Chga
Gcg
Hhex
Ins1
Ins2
Neurog3
Nkx6−1
Pdx1
Pecam1
Ppy
Sst
Ghrl
Pdgfra
Rgs5
Ccr5
Cd19
Ucn3
Iapp
Beta 1
Beta 2
Alpha
Delta
Immune B cells
Immune T cells
Other Immune cells
Vascular
Gamma
Stellate

Fig. S6. Single-cell RNA and ATAC characterization of Dec1 βKO mice.

(**A)** Clustering of single-cell gene expression profiles, assayed by RNA sequencing (left) and open chromatin profiles, assayed by ATAC sequencing (right), from isolated Dec1 βKO and littermate control islets, colored by sample of origin. Data are pooled from N= 2 WT and 2 Dec1 βKO mice, each sequenced separately.

(**B-C**) Quantification of open chromatin (B) and RNA (C) reads mapping to select marker genes for each cell cluster in (**Fig. 4E**).

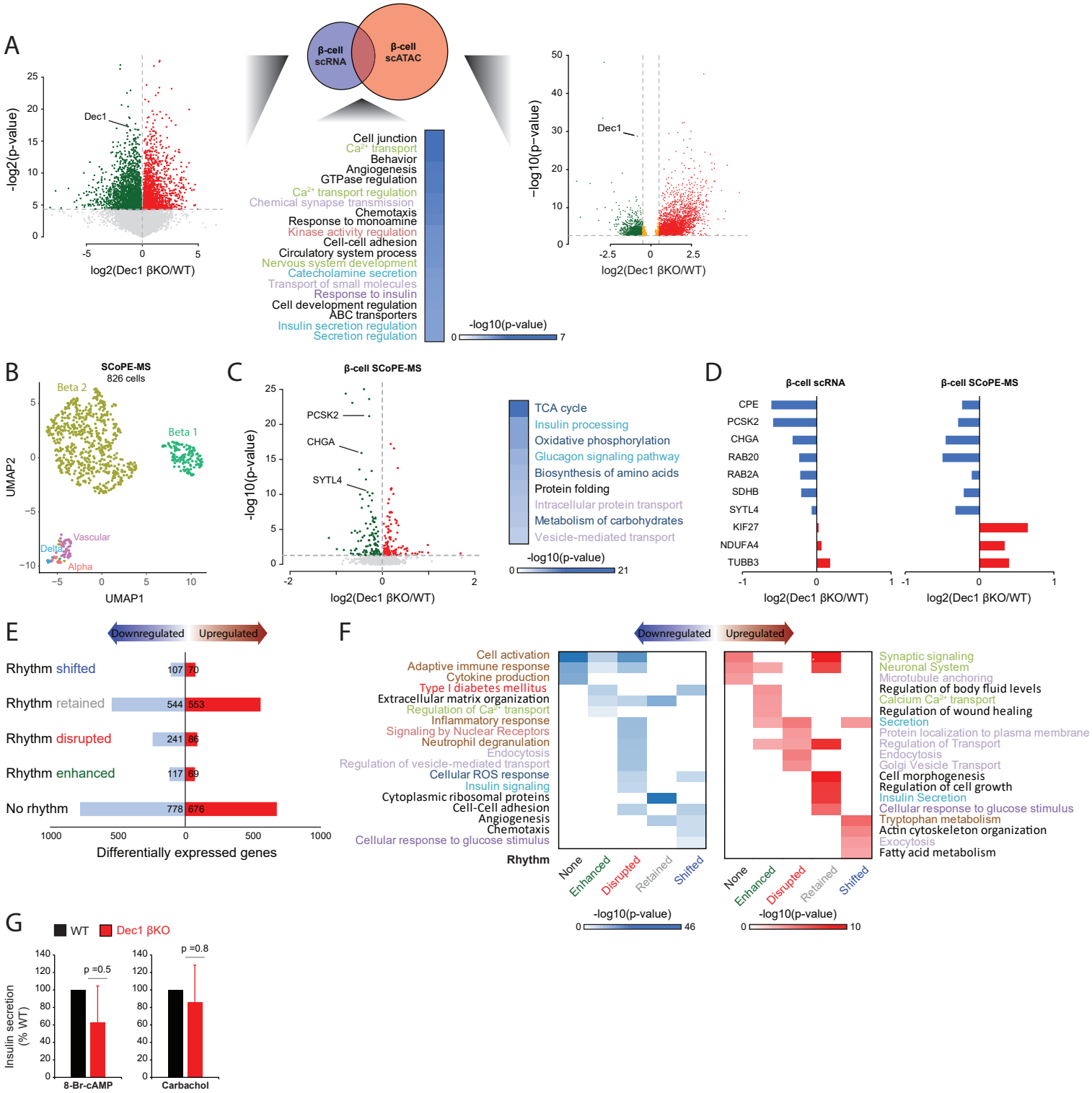
A
β-cell scRNA
β-cell scATAC
-log2(p-value)
log2(Dec1 βKO/WT)
Dec1
−log10(p−value)
Cell junction
Ca2+ transport
Behavior
Angiogenesis
GTPase regulation
Ca2+ transport regulation
Chemical synapse transmission
Chemotaxis
Response to monoamine
Kinase activity regulation
Cell-cell adhesion
Circulatory system process
Nervous system development
Catecholamine secretion
Transport of small molecules
Response to insulin
Cell development regulation
ABC transporters
Insulin secretion regulation
Secretion regulation
-log10(p-value)
B
SCoPE-MS
826 cells
Beta 2
Beta 1
Vascular
Delta
Alpha
UMAP2
UMAP1
C
β-cell SCoPE-MS
PCSK2
CHGA
SYTL4
-log10(p-value)
log2(Dec1 βKO/WT)
TCA cycle
Insulin processing
Oxidative phosphorylation
Glucagon signaling pathway
Biosynthesis of amino acids
Protein folding
Intracellular protein transport
Metabolism of carbohydrates
Vesicle-mediated transport
-log10(p-value)
D
β-cell scRNA
β-cell SCoPE-MS
CPE
PCSK2
CHGA
RAB20
RAB2A
SDHB
SYTL4
KIF27
NDUFA4
TUBB3
log2(Dec1 βKO/WT)
E
Downregulated
Upregulated
Rhythm shifted
Rhythm retained
Rhythm disrupted
Rhythm enhanced
No rhythm
107 70
544 553
241 86
117 69
778 676
Differentially expressed genes
F
Downregulated
Upregulated
Cell activation
Adaptive immune response
Cytokine production
Type I diabetes mellitus
Extracellular matrix organization
Regulation of Ca2+ transport
Inflammatory response
Signaling by Nuclear Receptors
Neutrophil degranulation
Endocytosis
Regulation of vesicle-mediated transport
Cellular ROS response
Insulin signaling
Cytoplasmic ribosomal proteins
Cell-Cell adhesion
Angiogenesis
Chemotaxis
Cellular response to glucose stimulus
Rhythm
None
Enhanced
Disrupted
Retained
Shifted
-log10(p-value)
Synaptic signaling
Neuronal System
Microtubule anchoring
Regulation of body fluid levels
Calcium Ca2+ transport
Regulation of wound healing
Secretion
Protein localization to plasma membrane
Regulation of Transport
Endocytosis
Golgi Vesicle Transport
Cell morphogenesis
Regulation of cell growth
Insulin Secretion
Cellular response to glucose stimulus
Tryptophan metabolism
Actin cytoskeleton organization
Exocytosis
Fatty acid metabolism
G
WT
Dec1 βKO
Insulin secretion (% WT)
p =0.5
p =0.8
8-Br-cAMP
Carbachol

Fig. S7. Deregulated glucose metabolism and glucose-dependent insulin secretion at the chromatin, transcription, and protein level in β-cells of Dec1 βKO mice.

(**A**) Gene expression (left) and chromatin accessibility (right) changes in β-cells from Dec1 βKO mice compared to littermate controls. Center: pathways enriched among genes deregulated at both the chromatin and transcription levels. Data are pooled from N= 2 WT and 2 Dec1 βKO mice, each sequenced separately.

(**B**) Clustering of single-cell protein expression profiles, assayed by SCoPE-MS, from isolated Dec1 βKO and littermate control islets. Data are pooled from N= 2 WT and 2 Dec1 βKO mice, each run separately.

(**C-D**) Proteome changes in β-cells from Dec1 βKO mice compared to littermate controls and pathways enriched among differentially regulated proteins (B). RNA and protein changes in β-cells for selected targets are shown in (C). Data are pooled from N= 2 WT and 2 Dec1 βKO mice, each analyzed separately.

(**E**) Distribution of genes differentially expressed in β-cells from Dec1 βKO mice among noncyclic or enhanced, disrupted, retained, or shifted rhythmicity models.

(**F**) Pathways enriched among noncyclic genes or genes with enhanced, disrupted, retained, or shifted rhythmicity that are downregulated (left) or upregulated (right) in Dec1 βKO mouse islets

(**G**) Glucose- and secretagogue-stimulated insulin secretion in size-matched islets isolated from *Dec1*-βKO mice and littermate controls. Data are mean ±SEM from N = 4 WT and 4 *Dec1*-βKO mice, each with n =2-3 replicate measurements, normalized to intracellular insulin content.